Supplementary Information

Emergent Neuro-mimetic Oscillations in Engineered Granular Assemblies

Ankur Bhaumik, Uddipan Ghosh, Hridesh Gupta, Navyashree Vasudeva, Parineeta Gogoi and Anshu Pandey*

Author Address

Solid State and Structural Chemistry Unit, Indian Institute of Science, Bangalore 560012, India

*Correspondence to

E-mail: anshup@iisc.ac.in

Contents

1. Synthesis

Chemicals: Zinc Oxide (ZnO, Thomas Baker, LR), Trioctylphosphine oxide(TOPO, Sigma Aldrich, Tech Grade, 90%), Titanium Oxide (TiO_2), Silver Chloride (AgCl, Permion, 99.997% metals basis), Stearic Acid (reagent grade, 95%)

1.1. ZnO nanoparticles (ZB)

2 g of commercially available ZnO was taken and mixed with 1 wt% of Trioctylphosphine oxide. The mixture was then ball milled for 2 hours using Tungsten Carbide WC balls of 4 mm diameter. The nanoparticles were then washed to remove excess ligands, centrifuged and dried.

1.2. TiO2 based nanoparticles (TB)

2 g of commercially available TiO_2 was taken and mixed with 1 wt% of stearic acid and 10 wt% of AgCl. The mixture was then ball milled for 2 hours using WC balls of 4 mm diameter. The nanoparticles were then washed to remove excess ligands, centrifuged and dried.

2. Structural Characterization of nanoparticles

2.1. TEM

2.1.1. ZnO nanoparticles (ZB)

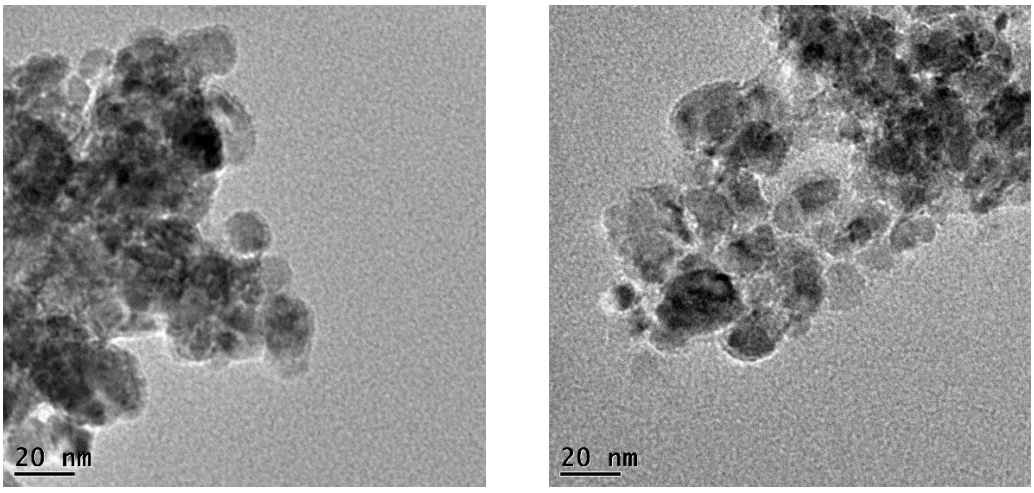

Figure S1: TEM images of synthesized ZB nanoparticles

The nanoparticles were suspended in acetone and drop cast on a Cu-C TEM grid for imaging. Images were taken with an accelerating voltage of 200kV. The images reveal that sizes of most particles have diameters in the range of 10 to 30 nm. These nanoparticles hierarchically assemble to form larger aggregates.

2.1.2. TiO2 based nanoparticles (TB)

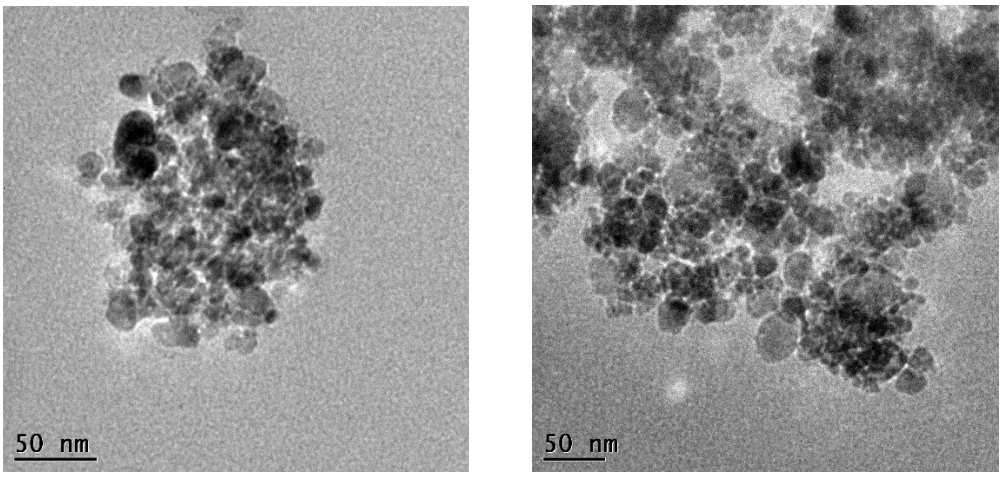

Figure S2: TEM images of synthesized TB nanoparticles

The nanoparticles were suspended in acetone and drop casted on a Cu-C TEM grid for imaging. Images were taken with an accelerating voltage of 200kV. The images reveal that sizes of most particles have diameters in the range of 10 to 50 nm. These nanoparticles hierarchically assemble to form larger aggregates.

2.2. SEM

2.2.1. ZnO nanoparticles (ZB)

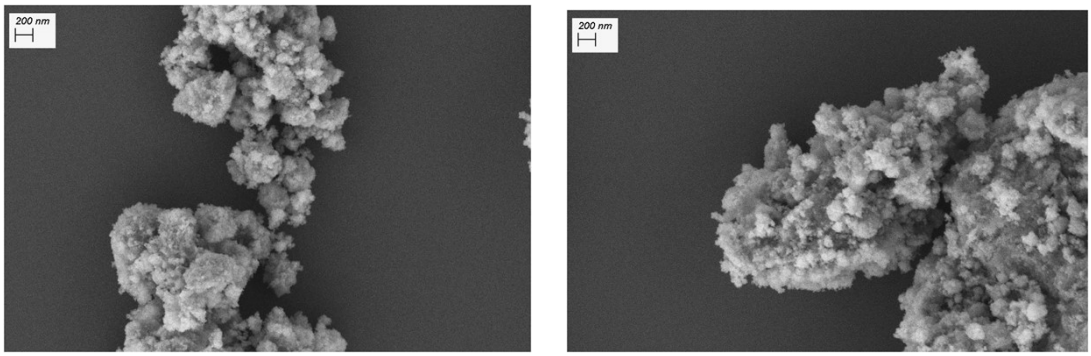

Figure S3: SEM images of synthesized ZB nanoparticles

The nanoparticles were suspended in acetone and drop casted on a Si – substrate for SEM imaging. Images were taken with a working distance of 8.8 mm and accelerating voltage of 5kV. The images show particles with random shapes. The sizes of these particles range from 100 to 500 nm. TEM images in the previous section reveal that these particles are aggregates of smaller particles.

2.2.2. TiO_2 based nanoparticles (TB)

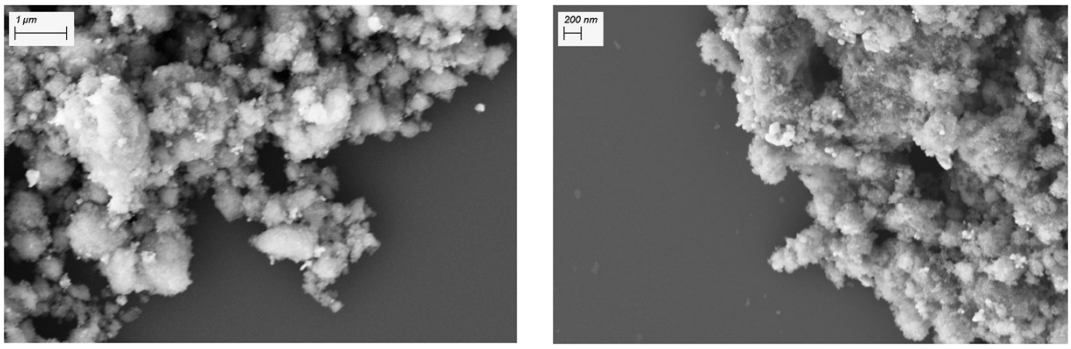

Figure S4: SEM images of synthesized TB nanoparticles

The nanoparticles were suspended in acetone and drop casted on a Si – substrate for SEM imaging. Images were taken with a working distance of 11 mm and accelerating voltage of 5kV. The images show particles with random shapes. The sizes of these particles range from 100 to 500 nm. TEM images in the previous section reveal that these particles are aggregates of smaller particles.

2.3. Powder XRD

2.3.1. ZnO nanoparticles (ZB)

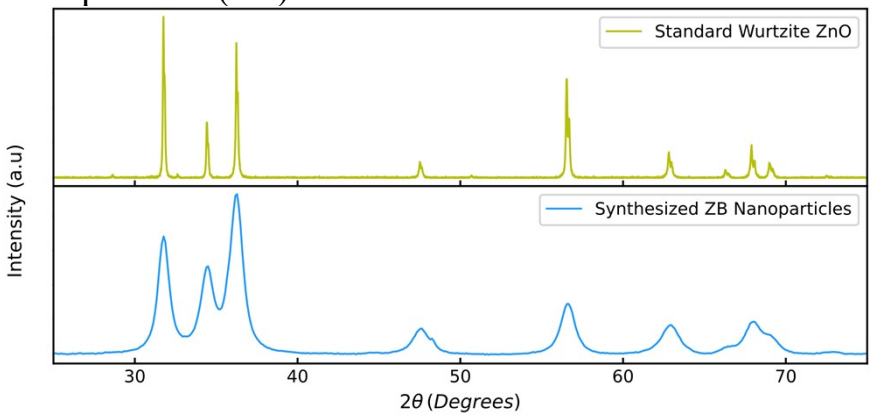

Figure S5: XRD spectra of synthesized ZB nanoparticles

XRD spectra of the synthesized ZB nanoparticles reveals that the ZnO is in Wurtzite phase.

2.3.2. TiO2 based nanoparticles (TB)

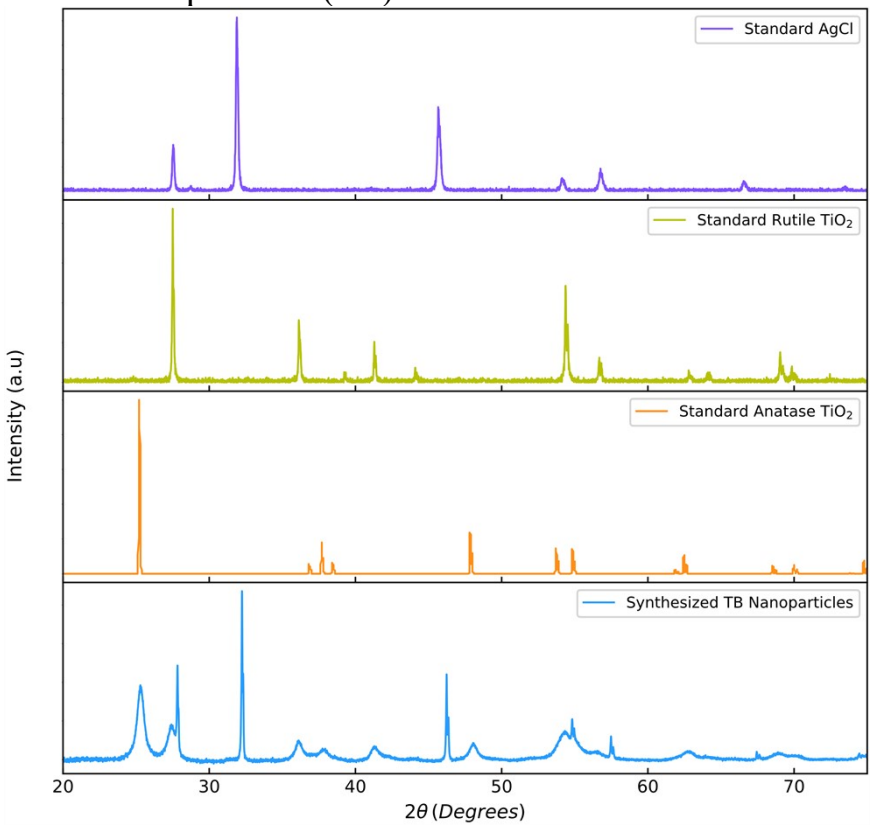

Figure S6: XRD spectra of synthesized TB nanoparticles

XRD spectra of the synthesized TB nanoparticles reveals that the synthesized TiO_2 is a mixture of rutile and anatase phases. Some unreacted AgCl is also present.

3. Device Preparation

Gold Electrodes were deposited on glass substrate using optical lithography and sputtering . Two geometries were used – 200 µm (**Figure S7**) and 2 µm (**Figure S8**). The 200 µm geometry was used for all measurements unless otherwise stated. The nanoparticles were dispersed in acetone and drop cast on the electrodes. The solvent was allowed to evaporate for 30 mins at 50 ℃. Electrical measurements on these devices were then performed.

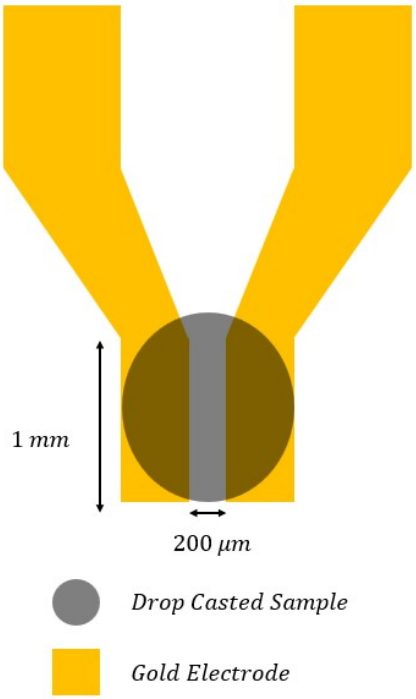

Figure S7: Schematic of the 200 µm electrode geometry

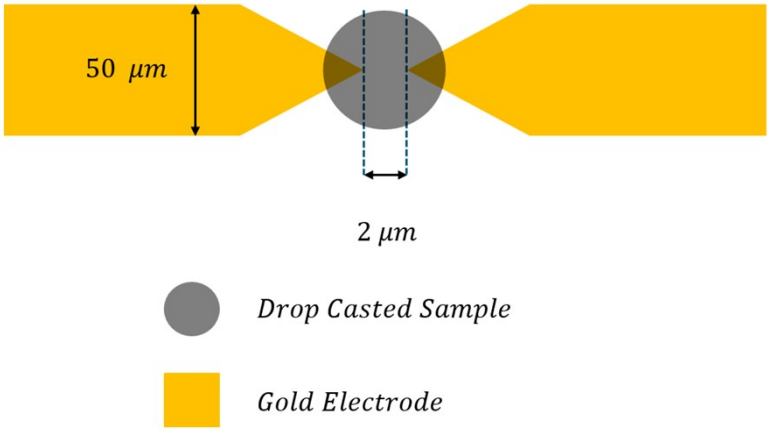

Figure S8: Schematic of the 2 µm electrode geometry

4. Device statistics and reproducibility 1 (ZB and TB)

The variation in device performance was studied and is described here -

4.1. ZB Devices

4.1.1. Device to device variation

11 devices were fabricated and the current was measured at a DC bias of 20V. In each case we found the current increases with time. The devices differ from each other in the time constant for the current to increase. 4 such representative time traces are shown in **Figure S9**.

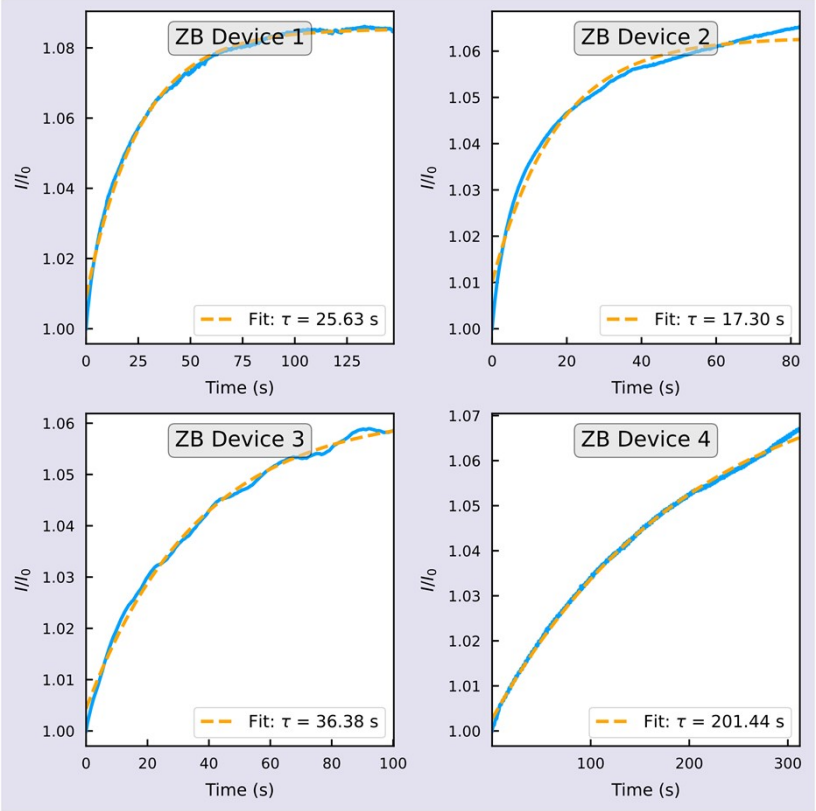

Figure S9: Representative time traces for 4 different ZB devices

4.1.2. Multiple measurements on ZB Device 3

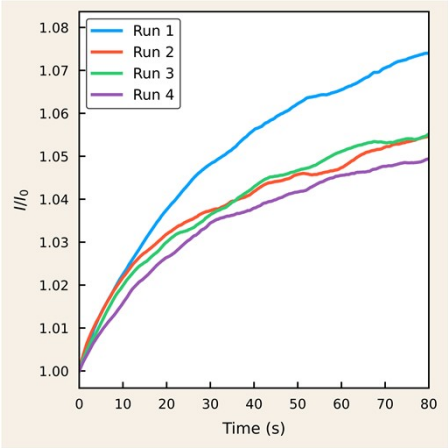

Figure S10: Time traces of multiple measurements on the same ZB device.

Current was measured for ZB Device 3 at a DC bias of 20 V multiple times (**Figure S10**). In all the cases the current increases with time.

4.2. TB Devices

4.2.1. Device to device variation

15 devices were fabricated and the current was measured at a DC bias of 20V. In each case we found the current decreases with time. The devices differ from each other in the time constant for the current to decrease. 4 such representative time traces are shown in **Figure S11**.

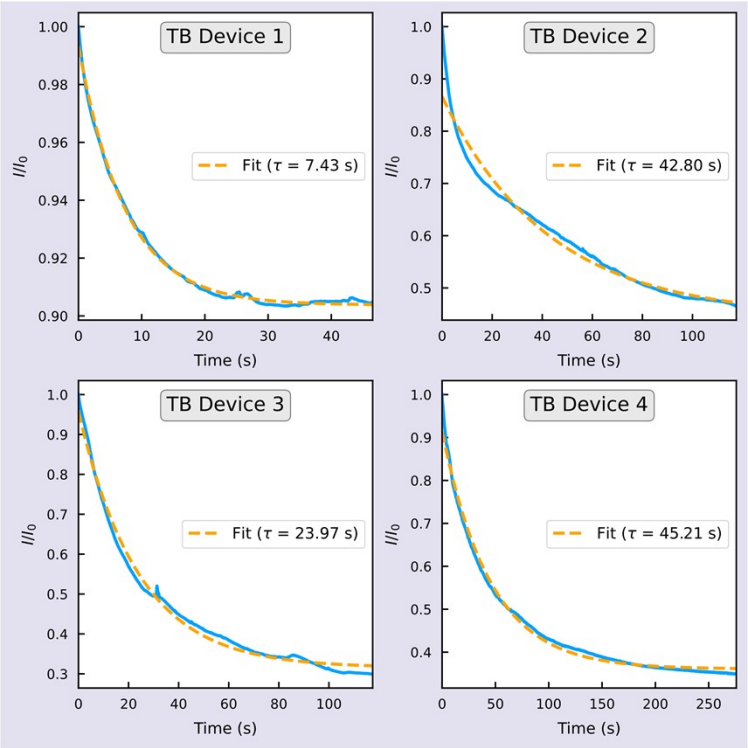

Figure S11: Representative time traces for 4 different TB devices

4.2.2. Multiple measurements on TB Device 2

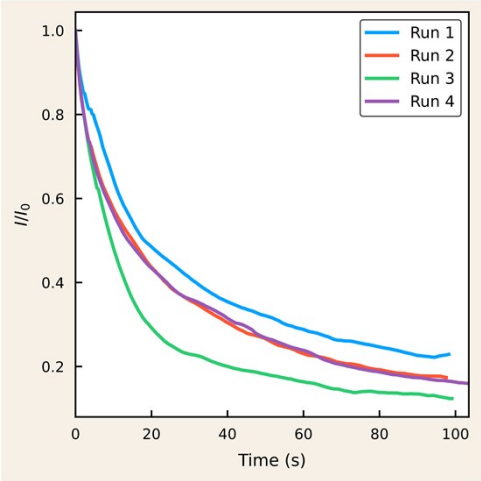

Figure S12: Time traces of multiple measurements on the same TB device.

Current was measured for TB Device 2 at a DC bias of 20 V multiple times (**Figure S12**). In all the cases the current decreases with time.

5. Measurement Setup

5.1. DC Measurements

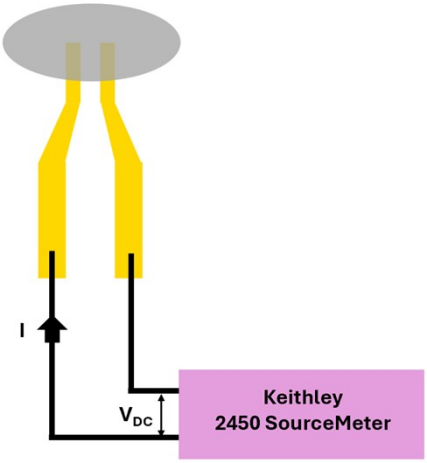

Figure S13: Schematic for DC measurements

The time-dependent current measurements under DC bias were carried out using a Keithley 2450 SourceMeter with a sampling rate of 10 Hz. A schematic of the measurement configuration is shown in **Figure S13**.

5.2. DC plus AC Measurements

For the memory experiments, both DC and AC bias voltages were applied. The DC bias was supplied using a Keithley 2450 SourceMeter, while the AC bias was generated using a Tektronix AFG31021 arbitrary function generator. The DC bias was applied between electrodes 1 and 3, and the resulting current was measured between the same electrodes using SourceMeter. The AC bias was applied independently between electrodes 2 and 4. A schematic representation of the experimental configuration is shown in **Figure S14**. Sampling rate of 10 Hz was used.

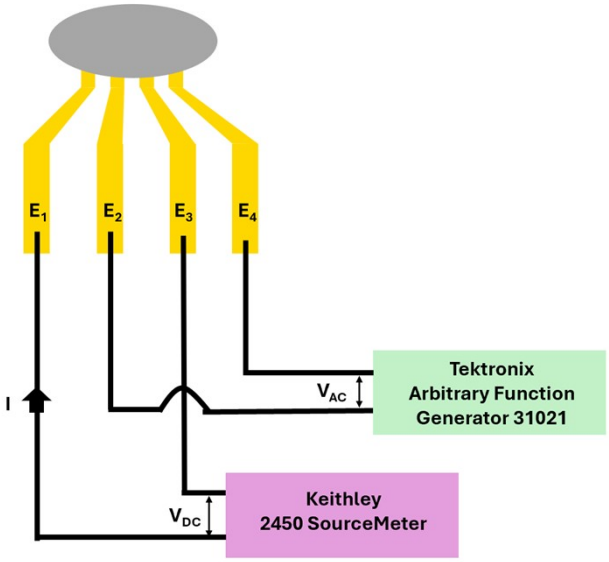

Figure S14: Schematic for DC plus AC measurements

6. Kinetic Monte Carlo Simulations of VRH

Due to computational limits, we restrict ourselves to a 2D simulation. We employ a lattice model for the nanoparticle film. The size of the system is set to 30 ($L = L_x = 30\ a$) sites (nanoparticles) in the x-direction and 30 ($L = L_y = 30\ a$) sites in the y-direction. Each site is assigned random zero field energies. For the ZB (TB) system the OFF-site energies are chosen in the range of 3 to $3.5kT$ (0 to $0.2kT$) away from the Fermi level where k is the Boltzmann constant and T is the temperature. The ON-site energies are chosen in the range of 0 to $0.2kT$ (3 to $3.5kT$) away from the Fermi level for the ZB (TB) system.

The hopping algorithm is the same as our previous work[1]. Briefly the algorithm works as follows. Localised states (sites) participating in the hopping conduction are represented by a square lattice. All distances are defined in terms of the lattice parameter a.

The periodic boundary condition of a torus is used, i.e.,

$$\Delta x = \min\left(|x_j - x_i|, L_x - |x_j - x_i|\right) \ldots (1)$$

$$\Delta y = \min\left(|y_j - y_i|, L_y - |y_j - y_i|\right) \ldots (2)$$

The energy difference between sites i and j incorporates the influence of the applied electric field F. It is given by:

$$\Delta E_{ij} = \Delta E_{ij\ no\ field} - Fe(x_j - x_i) \ldots (3)$$

where x_i is the coordinate of the centre of the site i along the direction of the field and e is the electronic charge.

At each simulation step, a pair of sites (i and j) is selected with a probability proportional to $e^{-\frac{2r_{ij}}{\varepsilon}}$ provided one site is occupied and the other is vacant. Whether the electron transitions between these sites is then determined by an energy-based acceptance criterion. The corresponding physical time increment for each accepted move is given by:

$$\Delta t = \tau_0 \left(\sum_i \sum_{j \neq i} e^{-2r_{ij}/\xi} \right)^{-1} \ldots (4)$$

where τ_0 is a system-dependent constant of the order of phonon frequency $10^{12}\ s^{-1}$. ΔE_{ij}, r_{ij} are the energy difference and distance between sites i and j respectively

After each Monte Carlo (MC) step, the system's total dipole moment P is updated. The electrical conductivity is then determined based on the time derivative of this dipole moment:

$$\sigma = \frac{1}{FL^2} \frac{dP}{dt} \ldots (5)$$

where σ is the conductivity.

Since, conductivity depends only on the rate of change of P, evolves over time, the simulation begins with $P = 0$. Whenever an electron hops in the direction of the applied electric field, P is incremented; if it hops against the field, P is decremented. In each case, the change in P is calculated as the electronic charge multiplied by the component of the hop distance aligned with the electric field. Before taking the derivative P was smoothened using a boxcar averaging over 1000-time bins.

At each KMC step an OFF-site which is occupied by an electron can switch ON with a probability $p_1 = 5 \times 10^{-6}$. Also at each KMC step an ON-site which is unoccupied by any electron can switch OFF with a probability $p_2 = 2 \times 10^{-6}$. As also mentioned in the main text it is not possible to perform simulations of experimental time scales. If VRH simulations are done over very short periods of time, there will be random fluctuations of current because the entire process is inherently stochastic. Averaging over a longer period will give an average value of current. Thus, the simulation times and the switching probabilities are chosen such that we can see a clear change in the conductivity of the system over a reasonably long simulation. The simulation is chosen to be long enough such that all random fluctuations get averaged out. This aspect has been discussed further in **SI Section 14.**

For the small 4×4 simulations the switching probabilities were reduced by a factor of 10^4. The timescale was also scaled by the same factor. This adjustment was necessary because, at such small scales, the inherent stochasticity of variable-range hopping (VRH) led to significant current fluctuations that precluded further analysis. By reducing the switching probabilities and averaging over a larger number of kinetic Monte Carlo (KMC) steps, these fluctuations were effectively minimized, allowing for a more stable and representative current response. This ensures that the current fluctuations seen in **Figure 5a** of main text are indeed due to the dynamic site energies and not an outcome of stochasticity associated with VRH simulations.

7. Conductive AFM

7.1. ZnO nanoparticles (ZB)

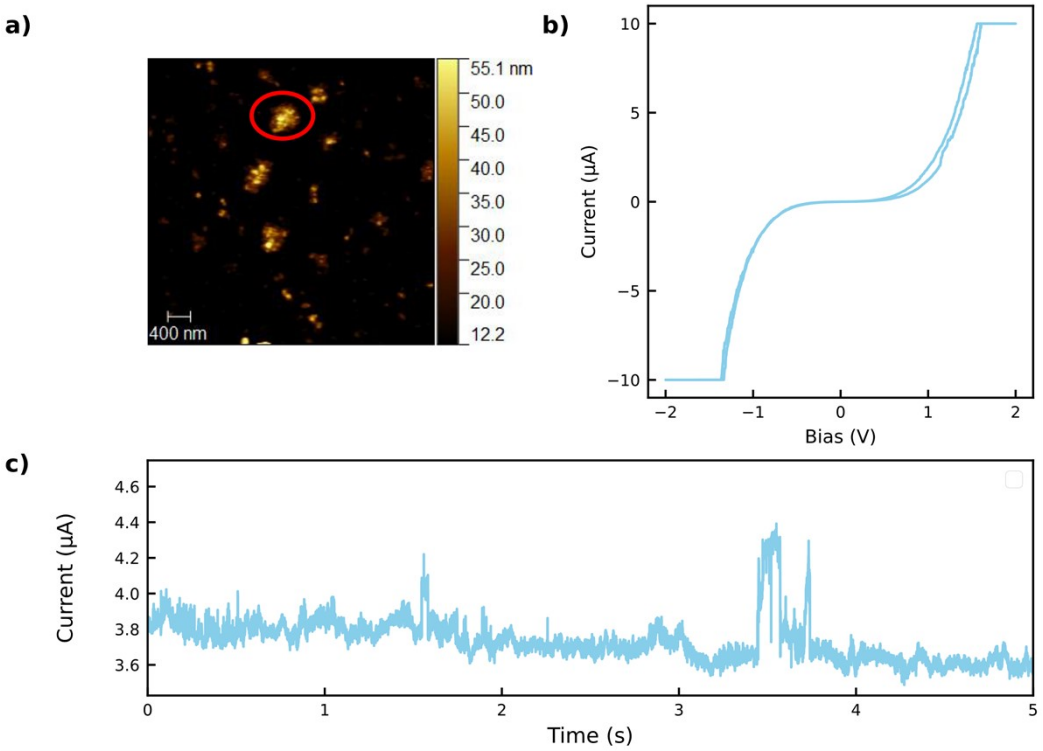

Figure S15: CAFM of ZB nanoparticles **a)** Height retrace of the scanned area **(b)** IV characteristic of the circled nanoparticle aggregate. **(c)** Current vs Time at a DC bias of 1.5 V

The ZB nanoparticles were deposited on a gold substrate. **Figure S15a** shows the height retrace of the surface in contact mode of AFM. A gold tipped AFM cantilever was used. Several nanoparticle aggregates are clearly visible. The AFM tip was taken to one such region (circled in red) and its electrical properties were studied. **Figure S15b** shows the representative IV characteristics. The measurement set-up cannot measure currents beyond $10\ \mu A$. Therefore, the current gets saturated at higher voltages. **Figure S15c** shows the current as function of time when a DC bias of 1.5V was applied. As can be seen the current changes randomly with time. Random changes in resistance in these and electrodic measurements have been modelled through the random switching of site energies in our VRH based model.

7.2. TiO_2 based nanoparticles (TB)

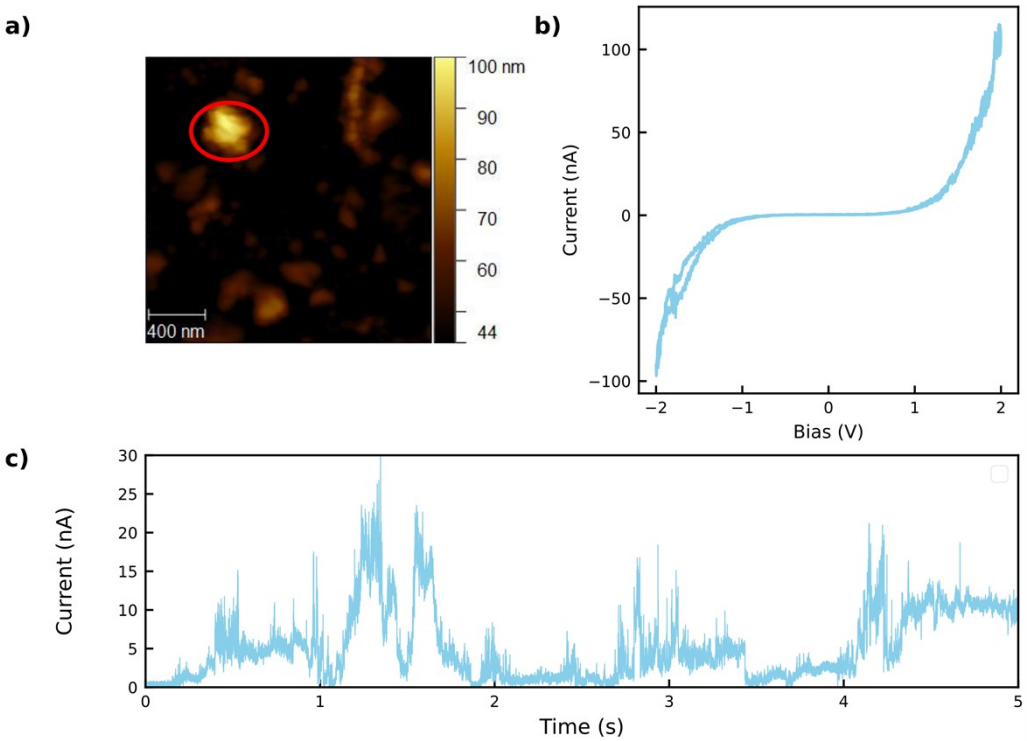

Figure S16: CAFM of TB nanoparticles **a)** Height retrace of the scanned area **(b)** IV characteristic of the circled nanoparticle aggregate. **(c)** Current vs Time at a DC bias of 1.5 V

Just like the ZB nanoparticles, TB nanoparticles were deposited on a gold substrate. **Figure S16a** shows the height retrace of the surface in contact mode of AFM. Gold AFM tip was once again used. Several nanoparticles are clearly visible. The AFM tip was taken to one such nanoparticles (circled in red) and its electrical properties were studied. **Figure S16b** shows the IV characteristics of a single nanoparticle. The curvature in the IV plot is once again due to the Schottky Junction formed at the metal (gold) – semiconductor (TiO_2) contact. **Figure S16c** shows the current as function of time when a DC bias of 2.5V was applied. As can be seen the current changes randomly with time. This random change in resistance of the nanoparticle has been modelled as the random switching of site energies in our VRH based model.

8. Investigation into the Mechanism of Conductivity Change

8.1. ZnO nanoparticles (ZB)

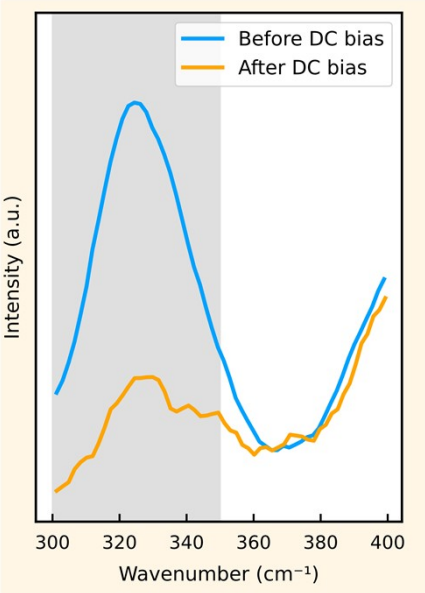

Figure S17: Raman Spectra of ZB before and after application of bias.

To understand the change in conductivity of ZB; we recorded the Raman spectra of the device film before and after the application of the DC bias (shown in **Figure S17**). We find that the peak in the 300 - 350 cm^{-1} disappears after the application of the bias. This peak is due to the second order mode ([2]). The disappearance of this peak implies the formation of oxygen vacancies and therefore a higher conductivity[3].

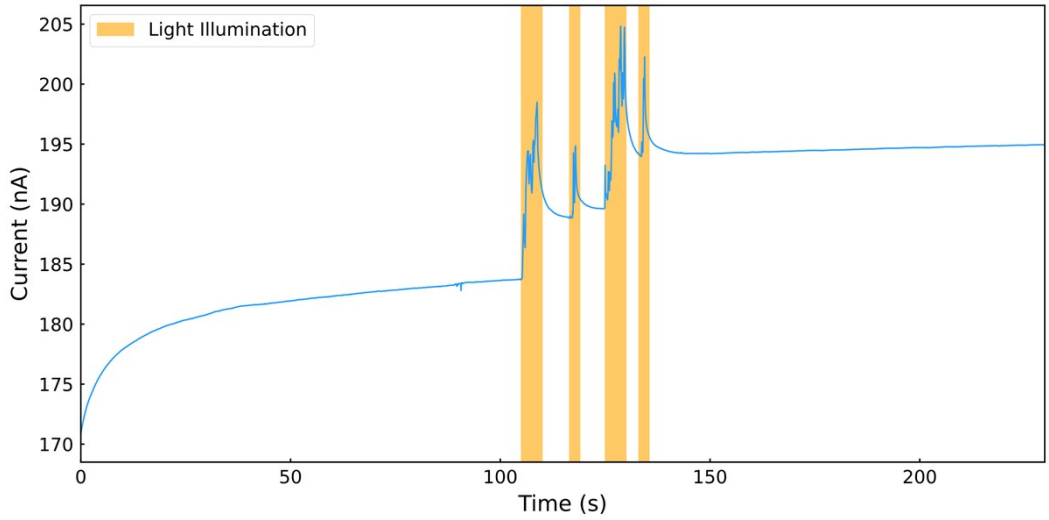

Figure S18: Effect of shining light on ZB device

Oxygen vacancies can also be created using light[4]. **Figure S18** shows the current as function of time when a DC bias is applied to ZB devices. In the highlighted regions the device was illuminated with light of wavelength 405 nm. During illumination there is an increase in the conductivity. This can be easily attributed to the excess photogenerated carriers. After the light is removed there is a permanent increase in conductivity. This is due to the creation of oxygen vacancies. Thus, this experiment supports that the increase in conductivity is due to oxygen vacancies.

8.2. TiO_2 based nanoparticles (TB)

To understand the change in conductivity of TB; we recorded the Raman spectra of the device film before and after the application of the DC bias (shown in **Figure S19**). The peak at $150\ cm^{-1}$ is the E_g mode of anatase. Application of additional DC bias leads to increase in Raman amplitude at $150\ cm^{-1}$. This is consistent with the partial conversion of a fraction of the rutile phase into anatase. Anatase has a higher band gap (3 eV) compared to rutile (2.52 eV)[5]. Our results thus suggest bias induced disruption of the TiO_2 lattice, accounting for reduced conductance. Observations of similar phase interconversion of TiO2 have been made by other authors[6,7].

9.

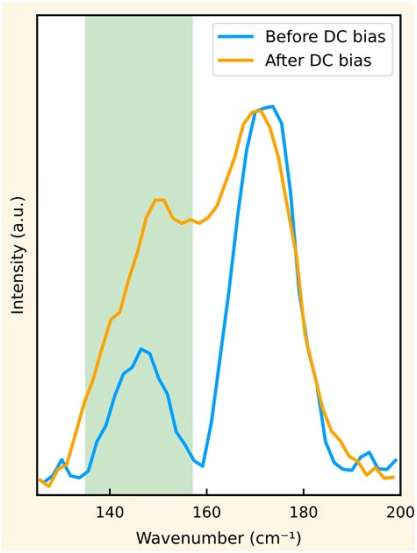

Figure S19: Raman Spectra of TB before and after DC bias

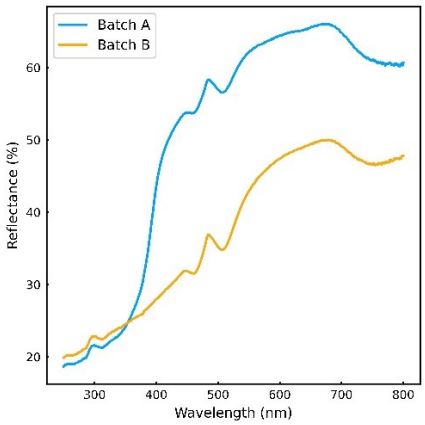

Figure S20: Comparison of Reflectance spectra of synthesized TB nanoparticles

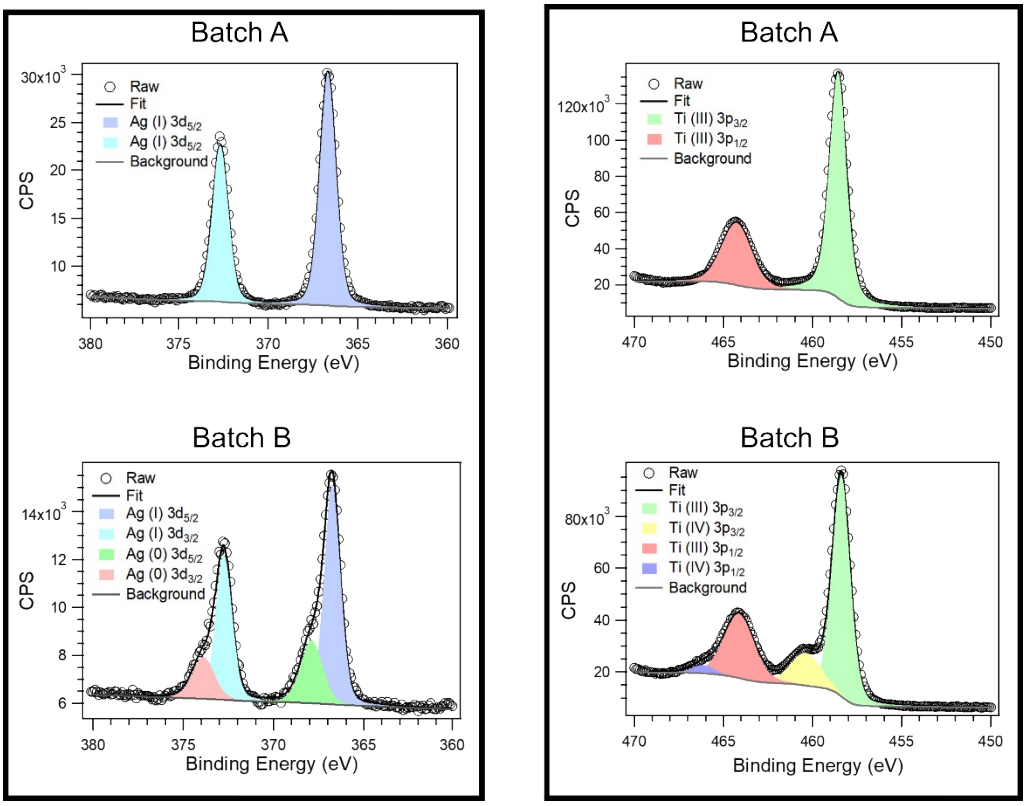

Figure S21: Comparison of XPS spectra of synthesized TB nanoparticles

Two batches of TB were synthesized. Batch A was prepared using the ordinary route, while for batch B, more aggressive (600 rpm) milling conditions were employed. Batch B shows significantly reduced optical reflectance compared to batch A (see **Figure S20**); this is attributed to side reactions of the silver precursors due to the synthetic conditions employed. It is found that Batch B fails to show oscillatory responses in all devices that were prepared, indicating the necessity of limiting side reactions of the silver precursors. To further understand our observations, X-ray Photoelectron Spectroscopic (XPS) studies were performed. Analysis of the XPS spectra (**Figure S21**) of these two samples reveals that in the Batch A Ag is in +1 oxidation state, and Ti is in +3 oxidation state. Literature reports[8] also show that doping TiO_2 with Ag^+ results in Ti^{3+} . In Batch B some Ag is present in 0 oxidation state and some Ti is present in +4 oxidation state. This suggests that the oxidation states (Ag^+ and Ti^{3+}) of the elements are important for the effect to be seen.

9. Noise Analysis of Experimental Set-Up

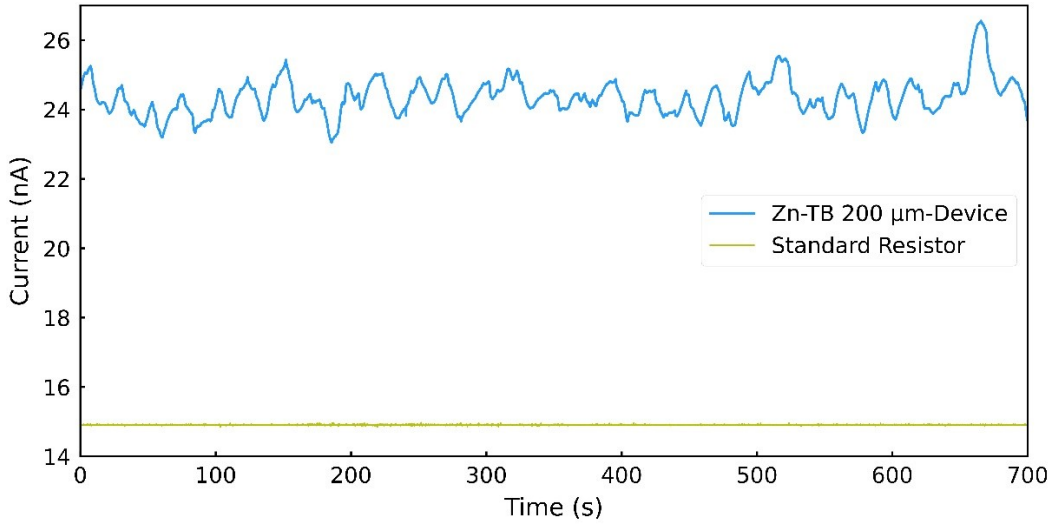

Figure S22: Comparison of the current oscillations in the ZB-TB 200 µm device with the noise level of the measurement system.

A DC bias was applied to a standard resistor and current as a function of time of was measured. As can be seen (**Figure S22**) the current oscillations for the Zn-TB 200 µm device is much larger than the noise in the measurement setup for this current range.

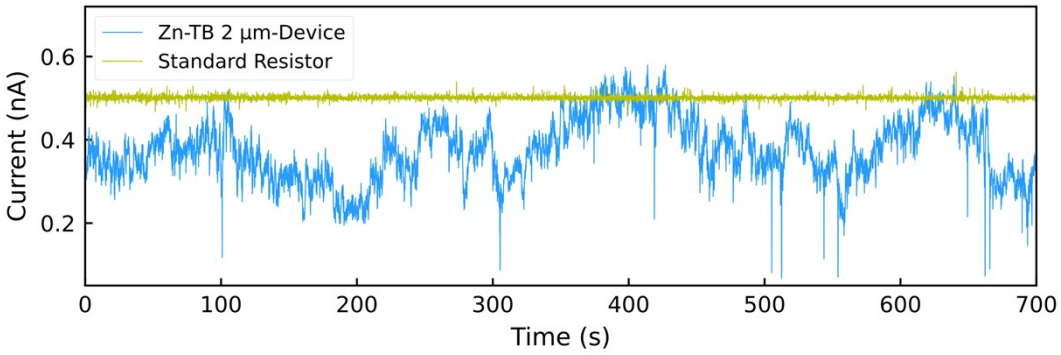

Figure S23: Comparison of the current fluctuations in the ZB-TB 2 µm device with the noise level of the measurement system.

A DC bias was applied to a standard resistor and current as a function of time of was measured. As can be seen (**Figure S23**) the current oscillations for the Zn-TB 2 µm is much larger than the noise in the measurement setup for this current range.

10. Device statistics and reproducibility 2 (ZB-TB Blend)

10.1 ZB-TB Blend 200 µm

i. Device to device variation

Total 23 devices were fabricated. Current was measured at a DC bias of 20V. All these devices show current oscillating with time with low spectral entropy. 10 such representative time traces are shown in **Figure S24** and **Figure S25**.

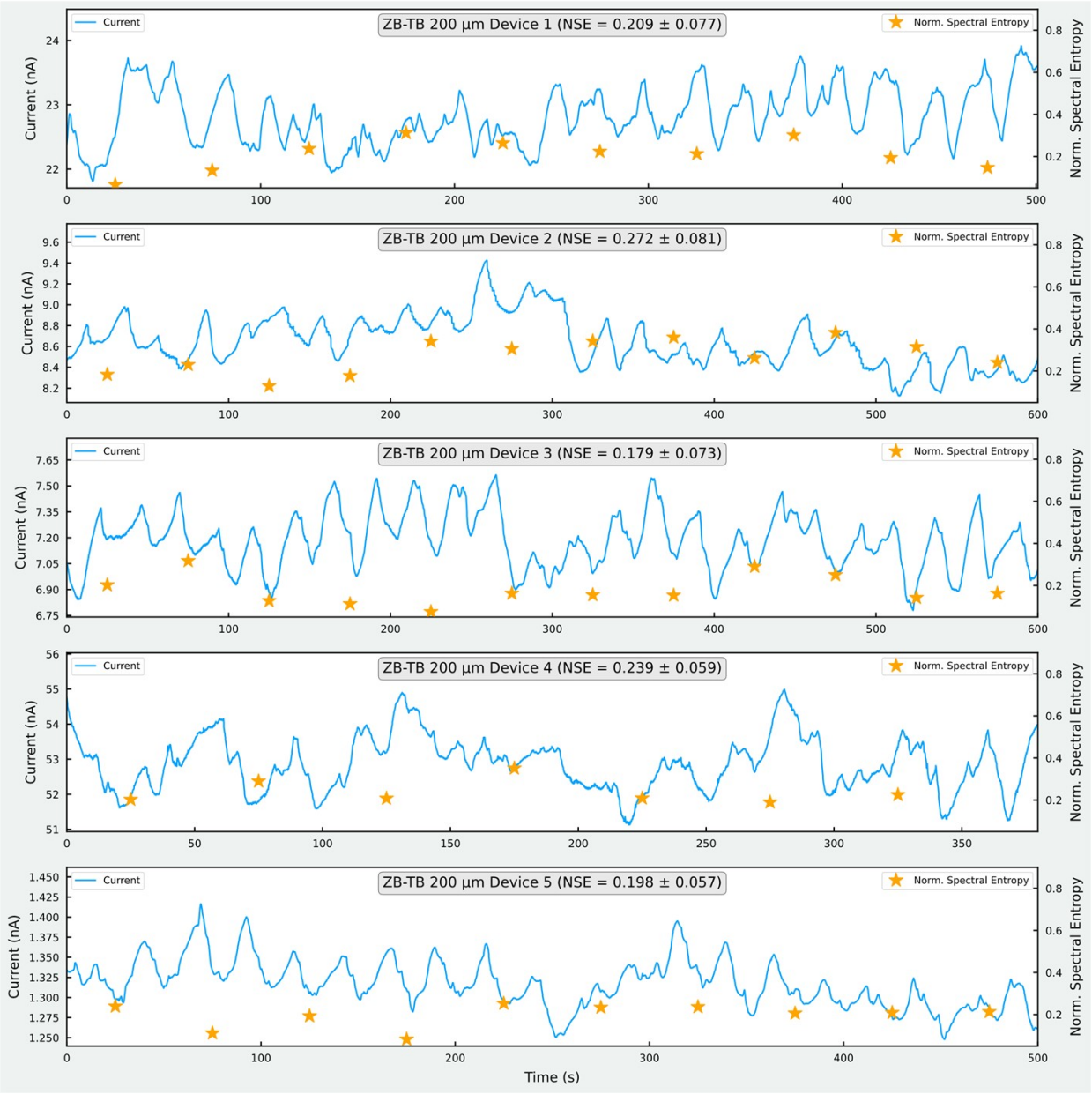

Figure S24: Representative time traces for 5 different ZB-TB Blend 200 µm devices

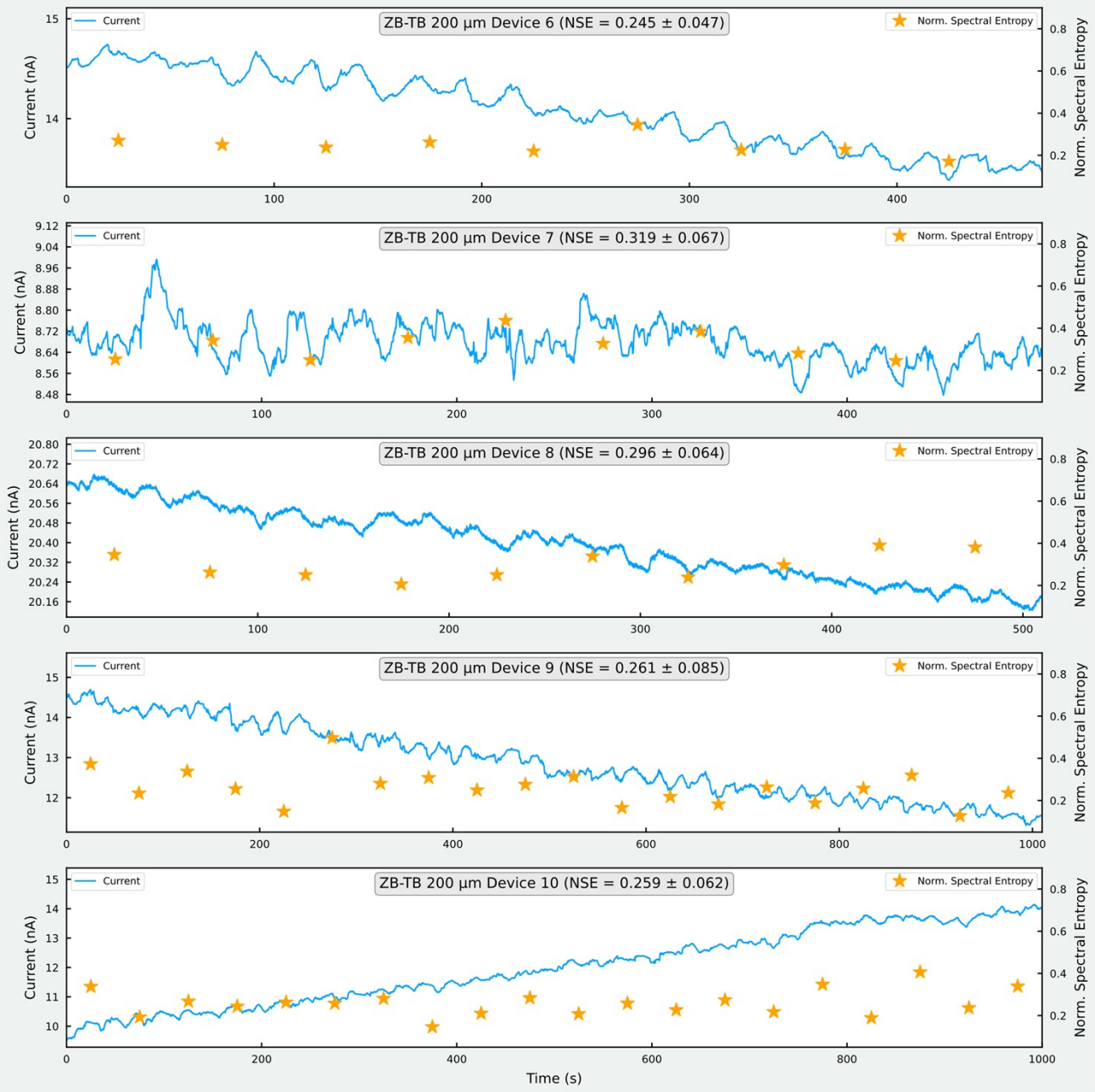

Figure S25: Representative time traces for 5 different ZB-TB Blend 200 µm devices

ii. Multiple measurements on ZB-TB 200 um Device 1

Current was measured for Device 2 at a DC bias of 20 V 3 times (**Figure S26**). In all the cases the current oscillates with time with low spectral entropy.

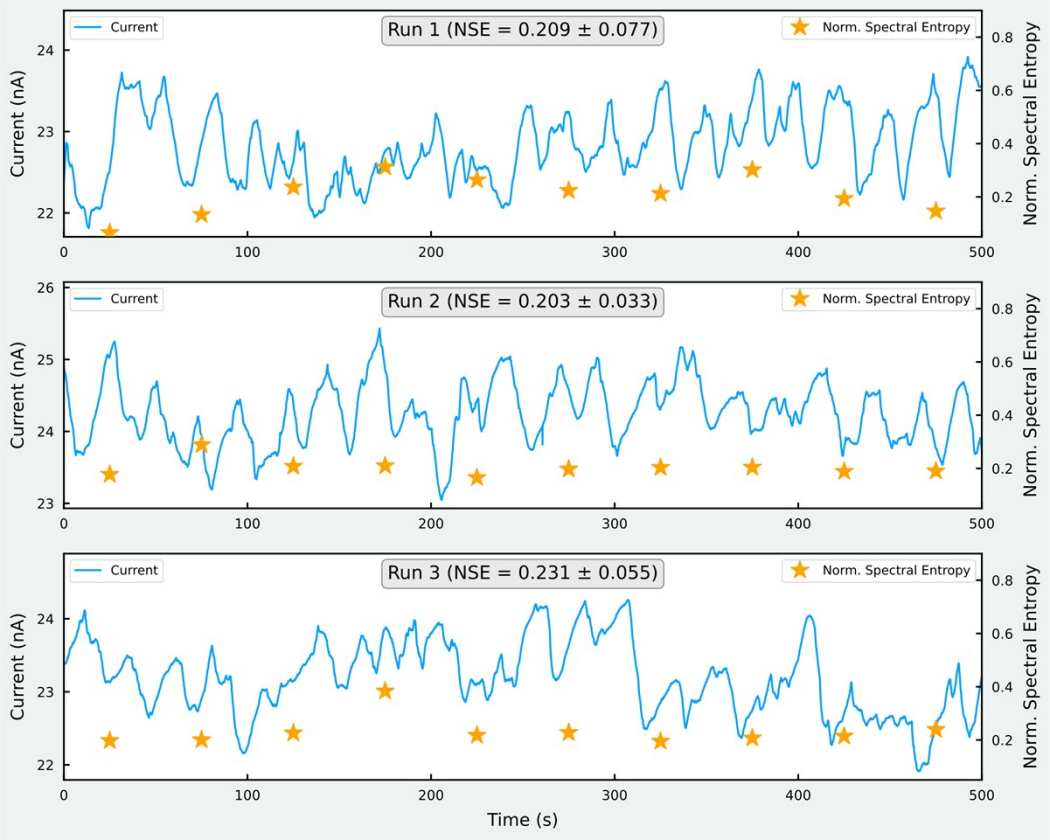

Figure S26: Time traces of multiple measurements on the same ZB-TB Blend 200 µm device.

10.2 ZB-TB Blend 2 µm

iii. Device to device variation

Total 9 devices were fabricated. All these devices show current fluctuating randomly with time with high spectral entropy.3 such representative time traces are shown in **Figure 27**. The devices differ only in the magnitude of the current.

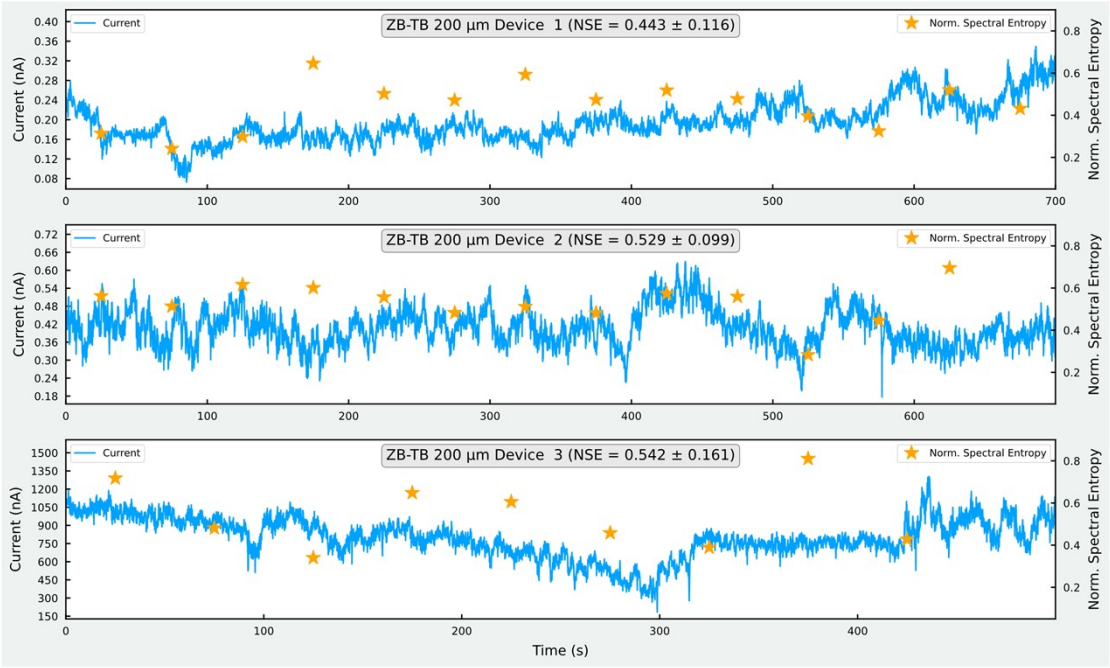

Figure S27: Representative time traces for 3 different ZB-TB Blend 2 µm devices

iv. Multiple measurements on ZB-TB 2 µm Device 2

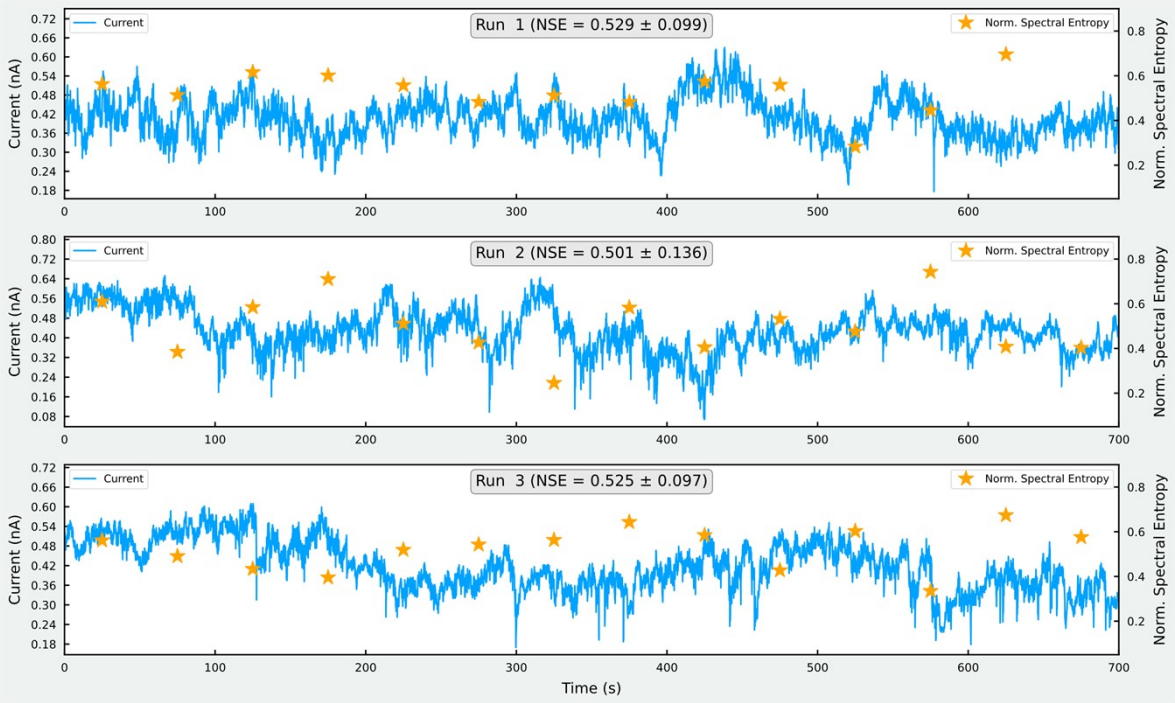

Figure S28: Time traces of multiple measurements on the same ZB-TB Blend 2 µm device.

Current was measured for Device 2 at a DC bias of 20 V 3 times (**Figure S28**). In all the cases the current fluctuates randomly with time with high spectral entropy.

11. Composition Space Study

A compositional phase space study was conducted for various TB–ZB ratios. At TB: ZB = 10:90, the mixture exhibits behaviour similar to that of pure ZB. Likewise, at TB: ZB = 90:10, the system behaves comparably to pure TB with no distinct oscillations. At intermediate compositions, distinct trends are observed. For TB: ZB = 33:67, the current increases with time, albeit with significant fluctuations. In contrast, for TB: ZB = 67:33, the current decreases with time, again accompanied by noticeable fluctuations.

These results indicate that the system tends to reflect the dominant component, while intermediate compositions exhibit competing effects that lead to increased fluctuations in the current. At a 50:50 composition, both components are present in equal proportions; consequently, the likelihood of observing oscillatory behaviour is maximized.

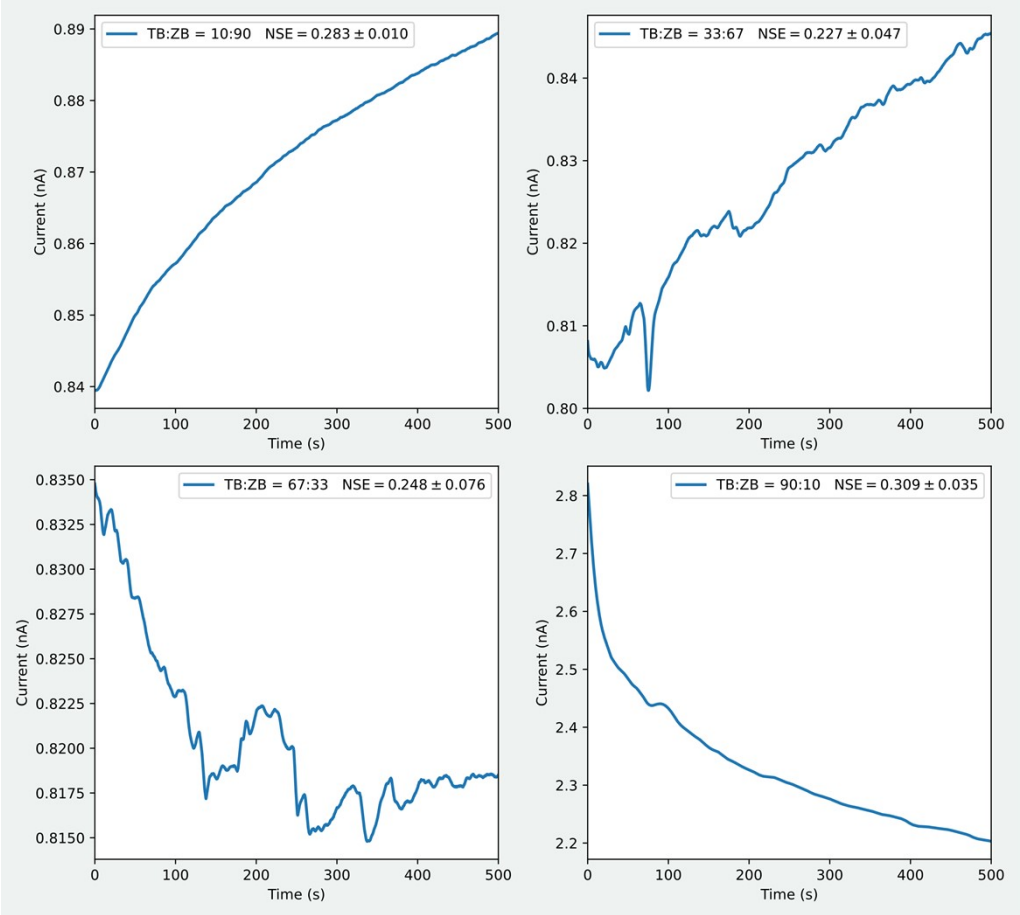

Figure S29: Variation in current with time for different TB:ZB ratios.

12. Normalised Spectral Entropy (NSE)

Mathematically Normalised Spectral Entropy is defined as follows:

Consider a signal $x(t)$ that varies with time.
Let $X(m)$ represent the discrete Fourier transform of the signal $x(t)$, where m is the frequency.
The power at each frequency m is given by the squared magnitude of the Fourier transform,
$S(m) = |X(m)|^2$.
The probability associated with each frequency component m is defined as the power at that frequency divided by the total power summed over all N frequency points:

$$P(m) = \frac{S(m)}{\sum_{i=1}^{N} S(i)}.$$

The spectral entropy H is calculated as the negative sum, over all frequency indices, of the probability at each frequency multiplied by the base-2 logarithm of that probability:

$$H = -\sum_{m=1}^{N} P(m) \log_2[P(m)].$$

Using this maximum value, the normalized spectral entropy can be written as the ratio of the actual entropy to the entropy of a uniform distribution:

$$H_n = \frac{-\sum_{m=1}^{N} P(m)\log_2[P(m)]}{-\sum_{m=1}^{N} \frac{1}{N}\log_2\left(\frac{1}{N}\right)}.$$

The time series was segmented into non-overlapping windows of 50 s duration. The normalized spectral entropy (NSE) was computed for each window, and the resulting values were used for further analysis. NSE calculations were performed using the AntroPy Python package. The analysis was restricted to the 0–6 Hz frequency range, and no additional noise filtering was applied.
The statistical analysis of NSE across devices is shown in **Figure S30**. It is found that for 200 µm devices the NSE lies in the range of 0.2 to 0.3. Whereas for 2 µm devices the NSE lies in the range of 0.45 to 0.55.

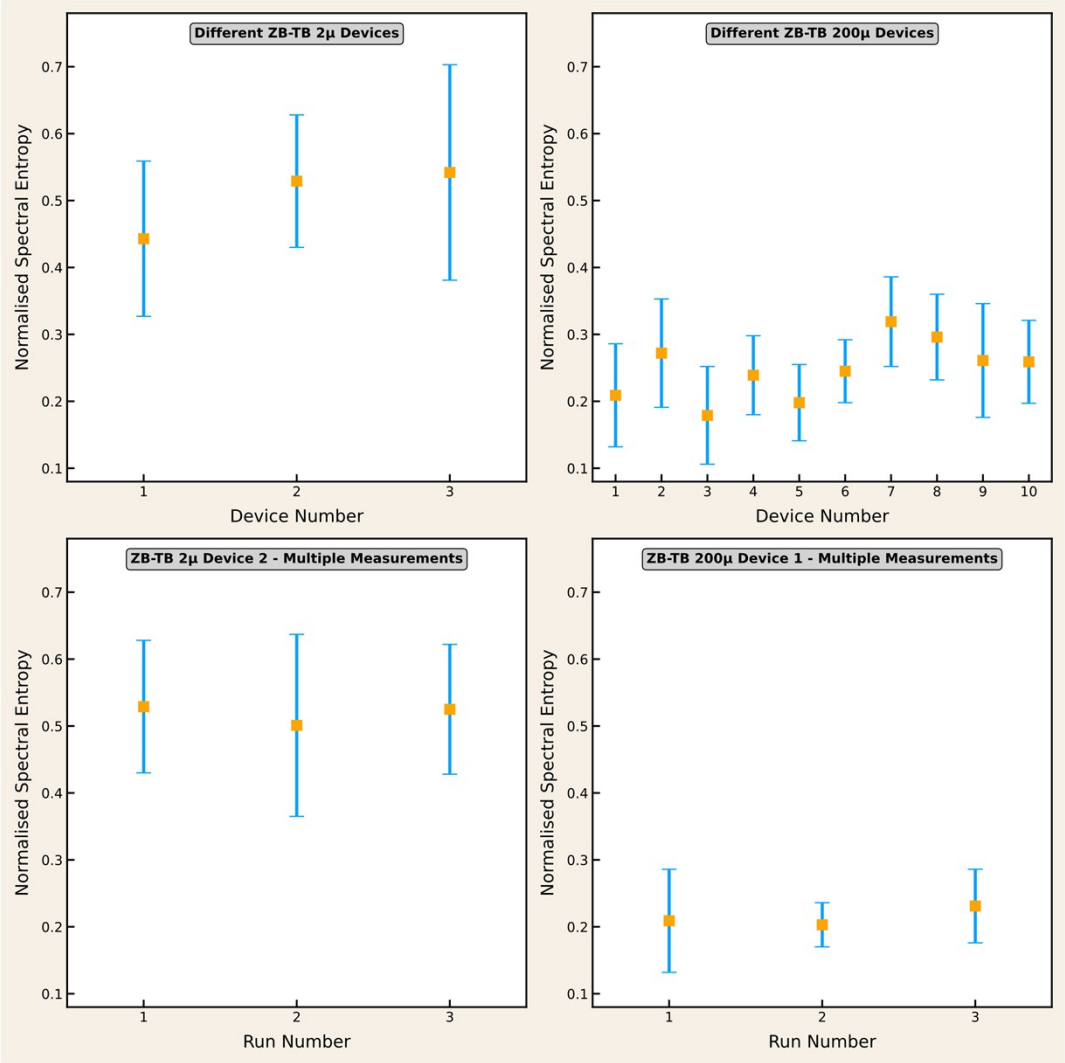

Figure S30: Variation in NSE for; **Top Right**: Different ZB-TB Blend 2µm device; **Top Left:** Different ZB-TB Blend 200µm device; **Bottom Left:** Multiple measurements on one single ZB-TB Blend 2µm device; **Bottom Right:** Multiple measurements on one single ZB-TB Blend 200µm device

13. Device Morphology

To understand if there are any morphological differences between the devices top view and cross-sectional SEM images of the device were collected. **Figure S31** shows the top-view SEM images of TB, ZB, TB-ZB blend 200 µm and TB-ZB blend 2 µm devices. As can be seen the films are continuous in the entire electrode gap region. As can be seen from the cross-sectional SEM (**Figure S32**) these films are of the order of 100 µm thick. This is consistent with the different properties of these devices arising from scaling properties and not due to the device structure.

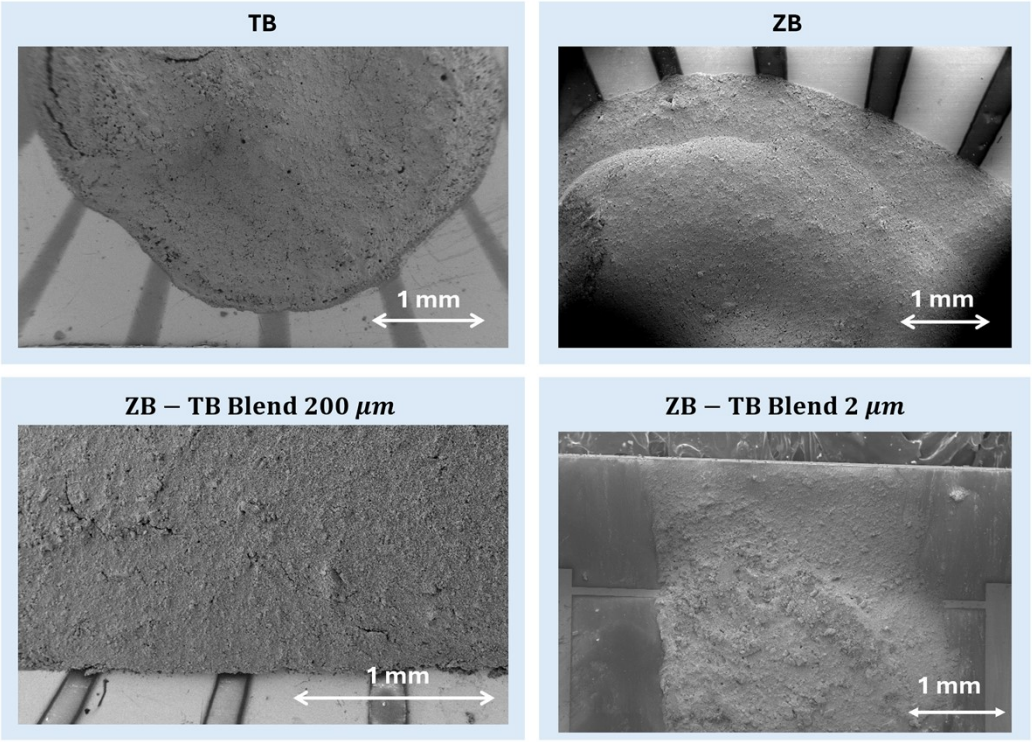

Figure S31: Top view SEM images of different devices **a)** TB **(b)** ZB **(c)** TB-ZB 200 µm device **(d)** TB-ZB 2 µm device

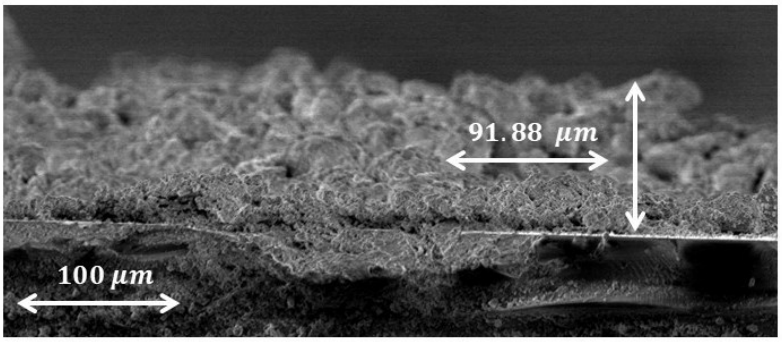

Figure S32: Cross sectional SEM image of device

Figure S33 shows the AFM height trace of the ZB, TB and ZB-TB blend device films and their RMS roughness values. We find that the RMS roughness lies in the range of 0.2-0.29% of the film thickness.

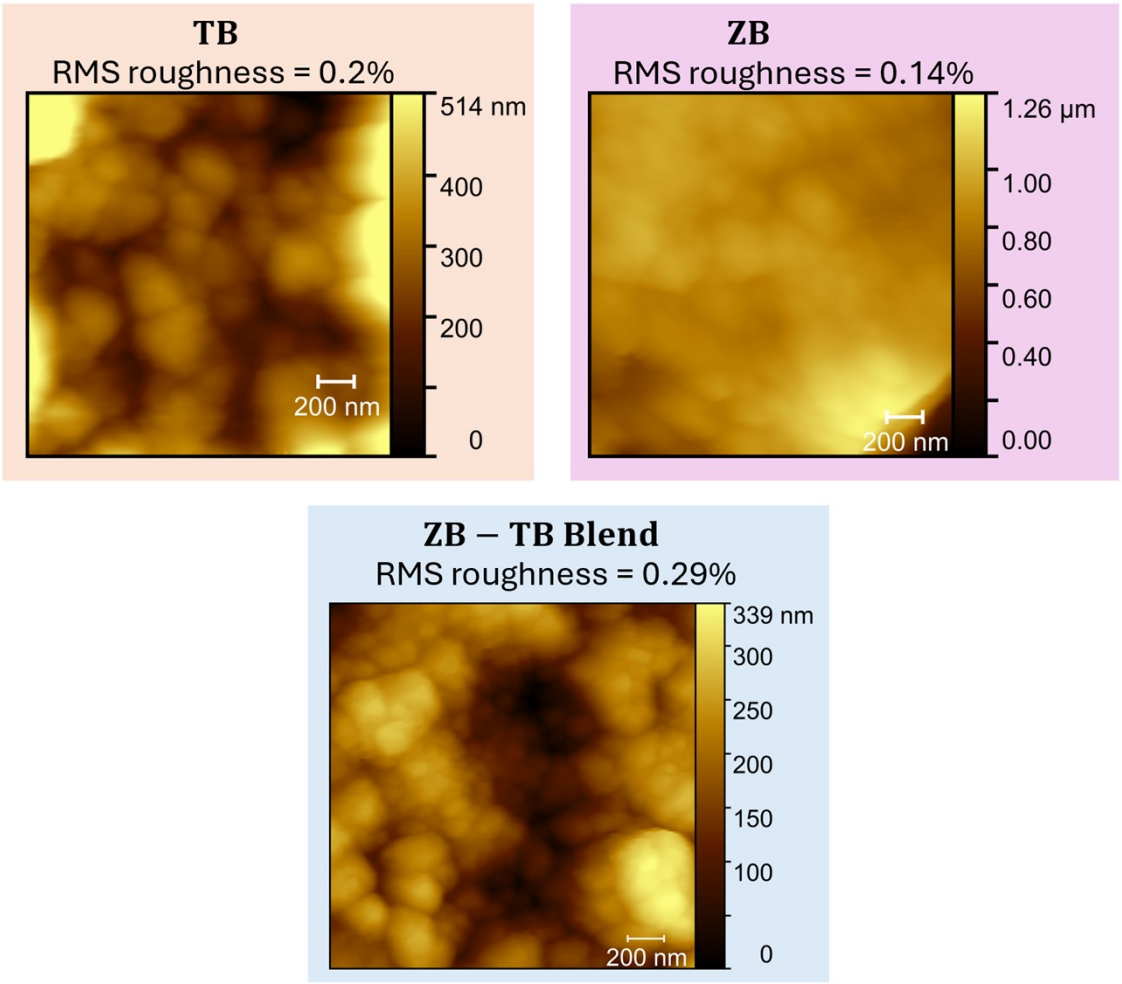

Figure S33: AFM height trace and RM roughness of devices.

14. Noise Analysis of VRH Simulations

In our model we have introduced dynamic site energies to explain the observed changes in conductivity with time. We found that the current changes with time in our simulations. As noted in the main text, VRH transport is inherently stochastic. Therefore, it is crucial to verify whether the fluctuations observed in simulations are due to the dynamic elements introduced in our model or due to the inherent stochasticity of the hopping process.

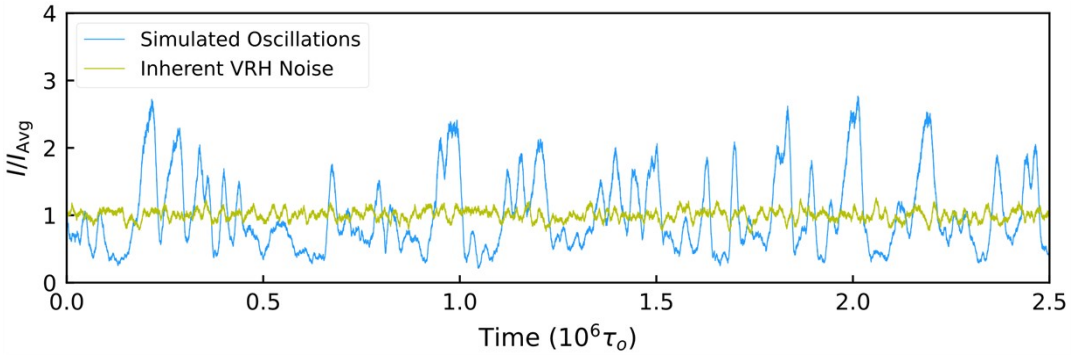

Figure S34: Comparison of the simulated current oscillations with the stochastic noise inherent in VRH simulations.

VRH KMC simulations were performed without any dynamic elements. **Figure S34** shows that the current fluctuations in the simulation with static site energies is much lower than the simulation with dynamic site energies. Thus, the oscillations observed in our simulations are indeed due to the dynamic elements introduced in our model.

15. Effect of Electrode Separation

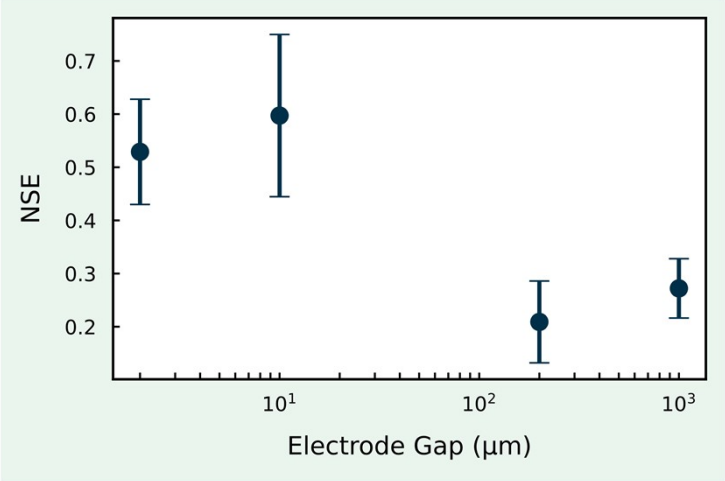

Figure S35: NSE variation with electrode gap.

Devices with electrode separations of 2µm, 10 µm , 200 µm and 1000 µm were prepared and the device response was measured. **Figure S35** shows the variation of NSE with electrode gap.

16. Effect of DC Bias on system behaviour

Device output was measured at different DC bias.

For the 200 µm device, oscillatory behaviour was observed at bias voltages of 10 V, 15 V, 20 V, and 30 V (**Figure S36a**), all characterized by low spectral entropy. The normalized spectral entropy (NSE) remains approximately 0.1-0.2 across all bias conditions (**Figure S36b**), indicating a consistently high degree of spectral order. More importantly, we observe changes to power spectral density (PSD), consistent with bias dependent control over the PSD of the devices. This is highlighted in **Figure S36c** and its inset.

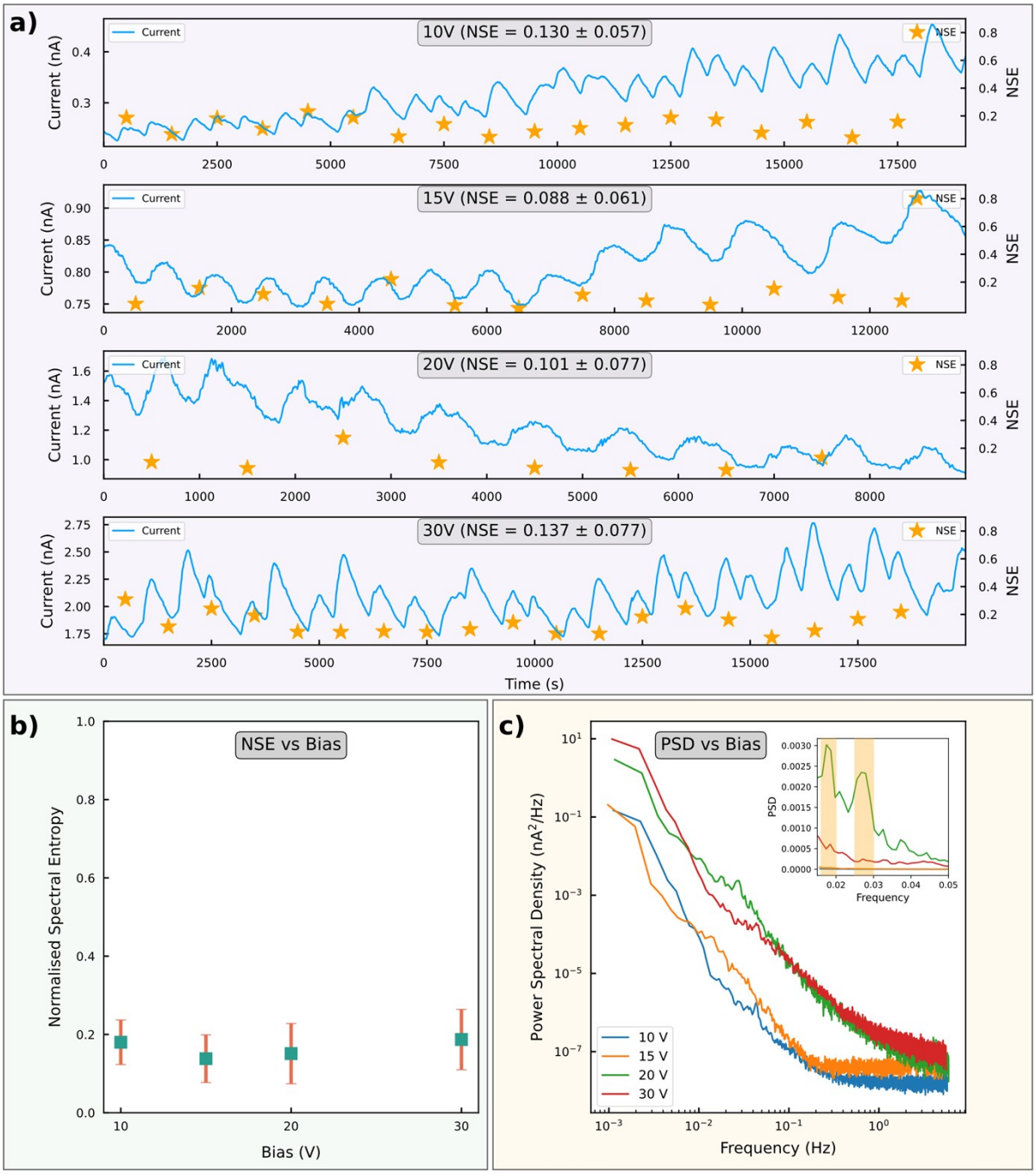

Figure S36: a) Time trace for ZB-TB blend 200 µm at different bias. **(b)** Comparison of their NSE **(c)** Comparison of their PSD. Inset: Zoomed in linear scale

For the 2 µm device, random fluctuations in current were observed at bias voltages of 15 V, 20 V, 30V and 40 V (**Figure. S37a**), all characterized by high spectral entropy(**Figure. S37b**). Further, we note that current does not increase linearly with the applied bias. The normalized spectral entropy (NSE) however remains approximately 0.5 across all bias conditions (**Figure S37c**), indicating a consistently lower degree of spectral order. The only notable variation in the power spectral density (PSD) occurs due to the different magnitude of current at different biases. However given its structural similarity and lack of identifiable features, we only attribute this to the mean current flowing through the devices.

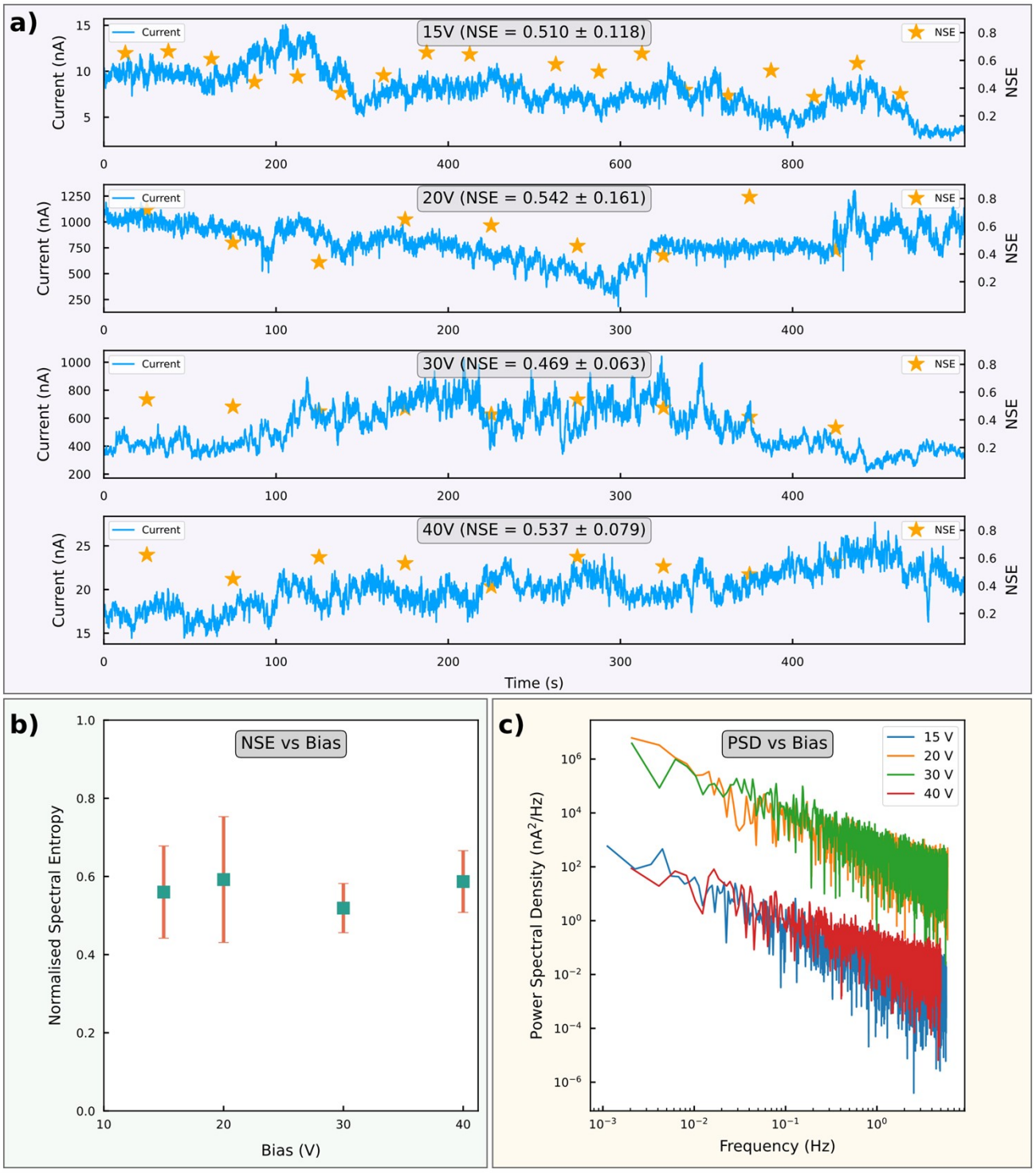

Figure S37: a) Time trace for ZB-TB blend 2 µm at different bias. **(b)** Comparison of their NSE **(c)** Comparison of their PSD.

17. Power Spectral Density (PSD)

Let $x(t)$ denote a signal that varies with time.
The discrete Fourier transform (DFT) of the signal $x(t)$ is represented as $X(m)$, where m is the frequency. The power associated with each frequency component is obtained by taking the squared magnitude of the DFT,

$S(m) = |X(m)|^2$. The power spectral density at frequency index m is defined as the power spectrum normalized by the product of the total number of frequency points and the sampling frequency,

$$PSD(m) = \frac{|X(m)|^2}{Nf_s}.$$ Here,

- N represents the total number of frequency points, and
- f_s denotes the sampling frequency of the original time-domain signal.

The power spectral density (PSD) was estimated using the Welch method, as implemented in the SciPy signal processing module (scipy.signal.welch).

18. Effect of frequency of AC bias on system oscillations.

The effect of different frequencies of AC bias on the system oscillations were also studied (**Figure S38**).

- When an AC frequency of 0.1 Hz was used, it was found that a new peak appears at 1.71 Hz and the peak at 3.24 Hz moves to a higher frequency.
- When an AC frequency of 0.2 Hz was used, it was found that the peak at 1.71 Hz shifts to a higher frequency and the peak at 3.24 Hz increases in magnitude.
- When an AC frequency of 0.3 Hz was used, it was found that the peaks at 3.25 Hz show changes in structure and relative weight, along with a redshift of the 1.71 Hz peaks.

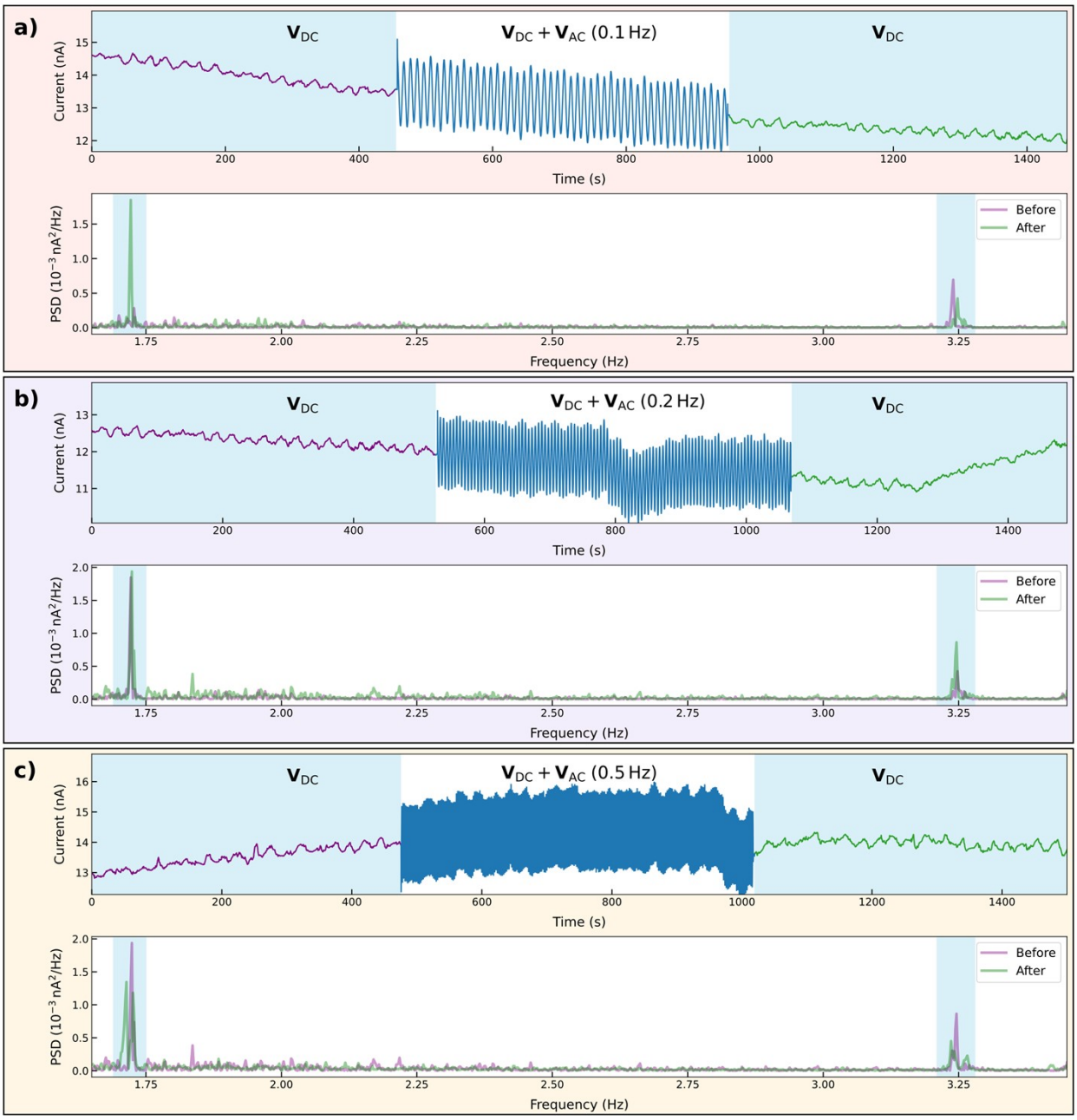

Figure S38: Effect of different AC frequency on the system oscillations **(a)** 0.1 Hz **(b)** 0.2 Hz **(c)** 0.3 Hz

19. Effect of amplitude of AC bias on system oscillations.

The effect of the amplitude of the AC bias was also studied (**Figure S39**).

- When a peak to peak voltage (V_{pp}) of 1 V was used we find that the peak at 1.75 Hz moves to a lower frequency and the peak at 3.18 Hz moves to 3.25 Hz.
- When a peak to peak voltage (V_{pp}) of 3 V was used we find that the peak at 1.75 Hz increases in magnitude.

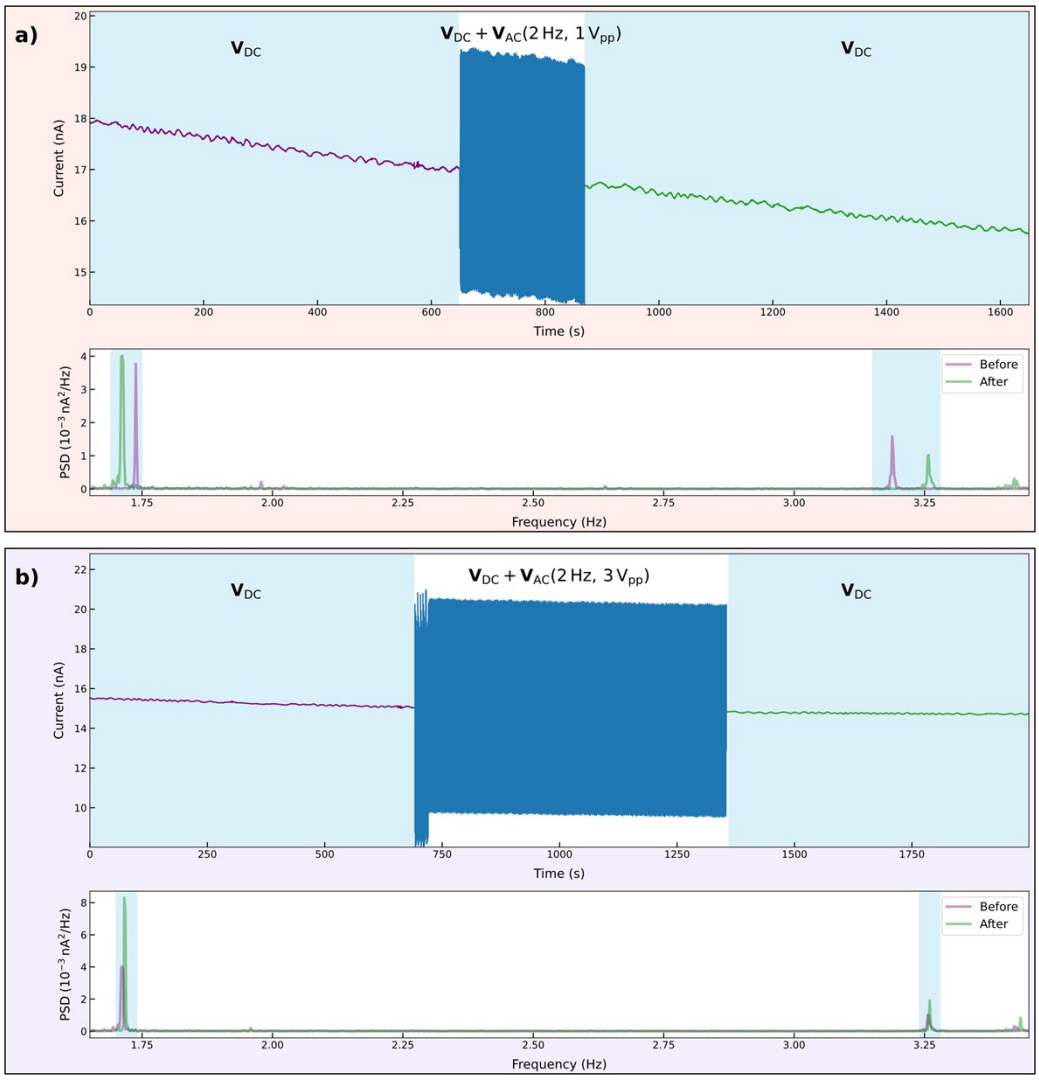

Figure S39: Effect of amplitude of AC bias on the system oscillations **(a)** $^{1}V_{pp}$ **(b)** $^{3}V_{pp}$

20. Effect of illumination on system oscillations.

The effect of illumination on the system oscillations were also studied. The system oscillations were recorded before and after illumination. No noticeable change was observed in the NSE (see **Figure S40**).

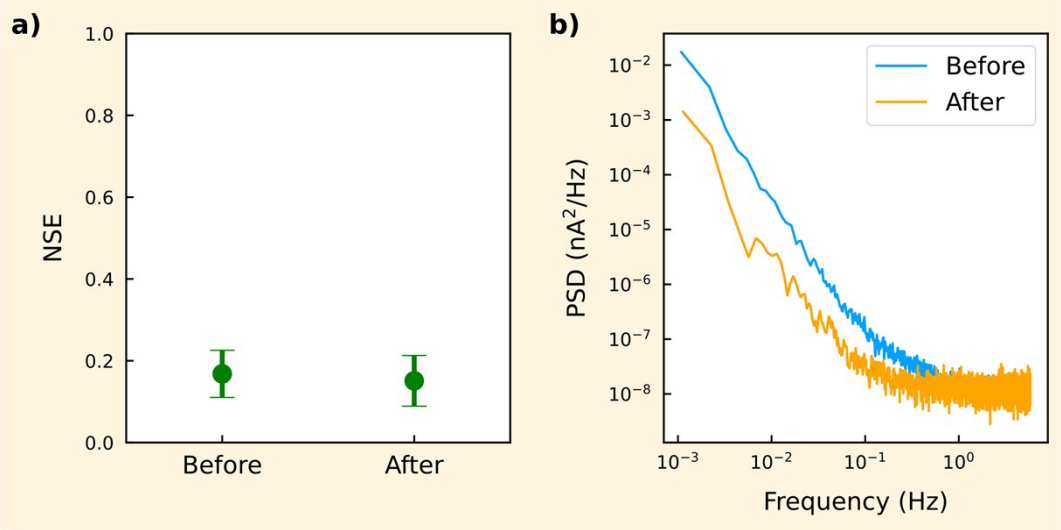

Figure S40: Effect of illumination on system oscillations – **(a)** NSE **(b)** PSD

21. Simulation of Memory Experiment

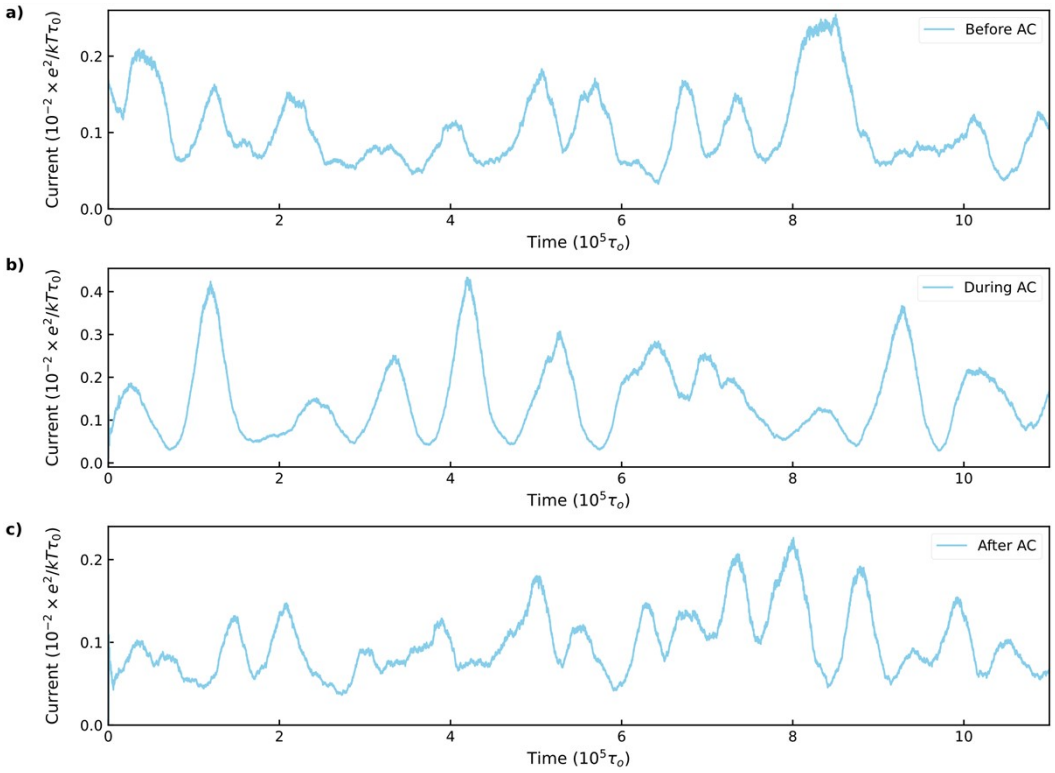

Figure S41: Simulated current as a function of time for the memory experiment. a) Before AC signal was applied (b) When AC signal was applied (c) After AC signal was applied.

First a DC electric field was applied. **Figure S41a** shows the simulated current for this period. After this an AC electric filed was applied. **Figure S41b** shows the simulated current for this period. Finally, a DC electric filed was applied. **Figure S41c** shows the simulated current for this period. **Figure 7c** in the main text compares the Fourier Transforms of these signals before and after the application of the AC signal.

22. References

1. *Bhaumik, A. & Pandey, A. Theoretical analysis of electron transport in perovskite thin films. Physical Chemistry Chemical Physics* ***26****, 25670–25677 (2024).*
2. *Fukushima, H. et al. Evaluation of oxygen vacancy in ZnO using Raman spectroscopy. in 2015 Joint IEEE International Symposium on the Applications of Ferroelectric (ISAF), International Symposium on Integrated Functionalities (ISIF), and Piezoelectric Force Microscopy Workshop (PFM) 28–31 (IEEE, 2015). doi:10.1109/ISAF.2015.7172660.*
3. *Ansari, S. A. et al. Oxygen vacancy induced band gap narrowing of ZnO nanostructures by an electrochemically active biofilm. Nanoscale* ***5****, 9238 (2013).*
4. *Gurwitz, R., Cohen, R. & Shalish, I. Interaction of light with the ZnO surface: Photon induced oxygen "breathing," oxygen vacancies, persistent photoconductivity, and persistent photovoltage. J. Appl. Phys.* ***115****, (2014).*
5. *Soussi, A. et al. Electronic and Optical Properties of TiO2 Thin Films: Combined Experimental and Theoretical Study. J. Electron. Mater.* ***50****, 4497–4510 (2021).*
6. *Sang, L., Zhao, Y. & Burda, C. TiO $_2$ Nanoparticles as Functional Building Blocks. Chem. Rev.* ***114****, 9283–9318 (2014).*
7. *Chen, X. & Mao, S. S. Titanium Dioxide Nanomaterials: Synthesis, Properties, Modifications, and Applications. Chem. Rev.* ***107****, 2891–2959 (2007).*
8. *Korduban, O. M., Kryshchuk, T. V., Kandyba, V. O. & Trachevskii, V. V. XPS studies of the surface of TiO2:Ag nanopowders. Himia, Fizika ta Tehnologia Poverhni* ***11****, 547–555 (2020).*